

# Fallback accretion on to a newborn magnetar: short GRBs with extended emission

S. L. Gibson,<sup>1</sup>★ G. A. Wynn,<sup>1</sup>★ B. P. Gompertz<sup>2</sup> and P. T. O’Brien<sup>1</sup>★

<sup>1</sup>*Department of Physics and Astronomy, University of Leicester, University Rd, Leicester LE1 7RH, UK*

<sup>2</sup>*Space Telescope Science Institute, 3700 San Martin Drive, Baltimore, MD 21218, USA*

Accepted 2017 June 14. Received 2017 June 7; in original form 2017 April 10

## ABSTRACT

There is a subset of short gamma-ray bursts (SGRBs) that exhibit a rebrightening in their high-energy light curves known as extended emission. These bursts have the potential to discern between various models proposed to describe SGRBs as any model needs to account for extended emission. In this paper, we combine fallback accretion into the magnetar propeller model and investigate the morphological changes fallback accretion has on model light curves and fit to the afterglows of 15 SGRBs exhibiting extended emission from the *Swift* archive. We have parametrized the fallback in terms of existing parameters within the propeller model and solved for the disc mass and angular frequency of the magnetar over time. We then apply a Markov chain Monte Carlo routine to produce fits to the data. We present fits to our extended emission SGRB sample that are morphologically and energetically consistent with the data provided by *Swift* Burst Alert Telescope and X-ray Telescope. The parameters derived from these fits are consistent with predictions for magnetar properties and fallback accretion models. Fallback accretion provides a noticeable improvement to the fits of the light curves of SGRBs with extended emission when compared to previous work and could play an important role in explaining features such as variability, flares and long dipole plateaux.

**Key words:** accretion, accretion discs – gamma-ray burst: general – stars: magnetars.

## 1 INTRODUCTION

Gamma-ray bursts (GRBs) are the brightest, most intense explosions in the Universe. They are very brief flashes of gamma-rays, lasting from a fraction of a second to several seconds, that occur at a rate of a few per day at random locations throughout the Universe (Mészáros 2006). GRBs are categorized based on a bimodal distribution in their temporal and spectral properties (e.g. Kouveliotou et al. 1993): long-soft GRBs and short-hard GRBs (SGRBs). The prompt emission of SGRBs typically lasts  $< 2$  s and their spectra are hard, whereas long-soft GRBs last  $> 2$  s and have softer spectra. However, this 2 s divide is not strict, e.g. Bromberg et al. (2013), and there is significant overlap between the two distributions including interesting phenomena such as the SGRBs with extended emission (SGRBEEs) discussed in this paper.

SGRBEEs are a subset of SGRBs which show rebrightening in high-energy light curves after the prompt emission spike (approximately 10 s after trigger), which is referred to as the extended emission (EE; Norris & Bonnell 2006). The peak flux of EE is usually lower than the initial spike but it can last for a few hun-

dred seconds, therefore the total fluence is often higher (Perley et al. 2009). They are believed to be a subset of SGRBs due to their hard spectra, association with galaxies with low-star-forming rates and the lack of any detectable supernovae coincident with the burst. These bursts are an interesting subset to study since any model hoping to describe SGRBs generally needs to account for those that exhibit EE and provide an argument as to why some bursts do not, or determine whether EE is just an observational artefact. Also, a model would need to explain EE energetically and account for the similar total energy in the EE and the prompt emission.

Different mechanisms have been suggested to power EE, including magnetar spin-down (Metzger, Quataert & Thompson 2008; Bucciantini et al. 2012), a two-jet solution (Barkov & Pozanenko 2011), fallback accretion (Rosswog 2007),  $r$ -process heating of the accretion disc (Metzger et al. 2010) and magnetic reconnection and turbulence (Zhang & Yan 2011). Previously, Gompertz, O’Brien & Wynn (2014) have implemented a propeller model with a magnetar central engine as an explanation for EE bursts. The magnetar is believed to be formed during the merger of two compact objects, i.e. a neutron star (NS) binary (Rosswog, Ramirez-Ruiz & Davies 2003; Belczynski et al. 2006), a white dwarf binary (Chapman et al. 2007) or an NS-white dwarf binary. Compact object binary mergers are also the most popular candidates for SGRB progenitors. Magnetars have proven to be a favourable central engine choice since

\* E-mail: [slg44@leicester.ac.uk](mailto:slg44@leicester.ac.uk) (SLG); [gwyy@leicester.ac.uk](mailto:gwyy@leicester.ac.uk) (GAW); [pto2@leicester.ac.uk](mailto:pto2@leicester.ac.uk) (PTO)

the energy released from their magnetic field via dipole spin-down is comparable to the energy contained within EE. The magnetic propeller model aims to extract the energy required for EE from mass ejected from the system via the propeller mechanism. The version presented in Gompertz et al. (2014) consists of a static disc that is fully formed at  $t = 0$  and is drained via either accretion or propelling. The results presented in Gompertz et al. (2014) run out of energy before fitting the fading afterglow, since the energy reservoir is not replenished, and does not fit to the prompt emission.

Models such as Rosswog (2007), Kumar, Narayan & Johnson (2008) and Cannizzo, Troja & Gehrels (2011) predict the fallback of mass into a disc and so the version of the propeller model presented here has been extended to include fallback accretion. This replenishes the disc and thereby increases the overall available energy budget within the model. This means that the mass of the disc can vary over time as opposed to the static disc presented in Gompertz et al. (2014) and affects the spin-up of the magnetar thereby changing the morphology of the light curves produced. This extension to the model will allow us to fit the prompt emission and retain enough energy to fit the fading afterglow where previous models could not. The fallback rate is modelled with a  $t^{-5/3}$  profile (Rosswog 2007) and the fallback time-scale, along with the available fallback mass, have been parametrized in terms of pre-existing parameters within the model. We aim to investigate the morphological changes that fallback introduces into the light curves and to explain the prompt emission (and hence all of the high-energy light curve) with a single model. As well as the addition of fallback mass and disc physics into the model, we have also introduced a new model for the propeller, fitted with variable efficiency parameters, and fitted to prompt emission data that were not included in Gompertz et al. (2014).

In Section 2, the mathematical theory of the propeller model is presented including: a discussion of significant changes applied for this paper, an exploration of the parameter space and a comparison with previous work by Gompertz et al. (2014). Section 3 introduces the sample of SRGBEs to be studied and Section 4 describes the method used to fit the model to the data. Discussed results and concluding remarks are presented in Sections 5 and 6, respectively.

## 2 MODEL DEVELOPMENT

Within the propeller model, the propeller regime is defined according to the relationship between the Alfvén radius (the radius at which the dynamics of the gas within the disc is strongly influenced by the magnetic field,  $r_m$ ) and the co-rotation radius (the radius at which material in the disc orbits at the same rate as the magnetar surface,  $r_c$ ). These radii are defined as follows:

$$r_m = \mu^{4/7} (GM)^{-1/7} \left( \frac{3M_D(t)}{t_v} \right)^{-2/7}, \quad (1)$$

$$r_c = (GM/\omega^2)^{1/3}, \quad (2)$$

where  $\mu$  is the magnetic dipole moment of the central engine,  $G$  is the gravitational constant,  $M$  is the mass of the central engine,  $M_D(t)$  is the disc mass at any given time,  $\omega$  is the angular frequency of the central engine and  $t_v$  is the viscous time-scale that is given by  $t_v = R_D/\alpha c_s$ . Here,  $R_D$  is the disc radius,  $\alpha$  is a viscosity prescription and  $c_s$  is the sound speed in the disc. We have used  $\alpha = 0.1$  and  $c_s = 10^7 \text{ cm s}^{-1}$  throughout this work, in keeping with Gompertz et al. (2014).

When  $r_c > r_m$ , the accretion disc is rotating more rapidly than the magnetic field (assuming the magnetic field rotates rigidly with the magnetar surface) and magnetic torques act to slow the infalling material down and allow it to accrete. In this case, the magnetar gains angular momentum and spins up hence the rotation of the field increases. Conversely if  $r_c < r_m$ , the magnetic field is rotating faster than the material and the result is that particles are accelerated to super-Keplerian velocities and ejected from the system. The magnetar loses angular momentum to the ejected material and its rotation is slowed. This is the propeller regime. To prevent the ejected material from exceeding the speed of light,  $r_m$  is capped at a fraction of the light cylinder radius  $r_{lc}$ , which is the radius at which the magnetic field lines rotate at the speed of light in order to maintain rigid rotation with the stellar surface. It is difficult to determine where effective coupling between the magnetic field and the plasma breaks down. We have therefore used a conservative estimate of  $r_m = 0.9r_{lc}$  in common with Gompertz et al. (2014) that allows comparison with their results.

The theory behind the magnetic propeller model is largely based on that presented in Piro & Ott (2011) and Gompertz et al. (2014). Therefore, a full description of the model equations will not be presented here and the focus will remain on the amendments required to model fallback accretion. We have assumed the accretion disc has a surrounding mass budget available to fallback smoothly on to the outer radius of the disc on a ballistic time-scale of  $t^{-5/3}$ , in line with models such as Rosswog (2007), and mass flows from the inner disc towards the magnetar with an exponential profile.

The radii  $r_m$  and  $r_c$  are dependent on the mass of the accretion disc and the rotation frequency of the magnetar. We have modelled the change in disc mass and frequency with the following equations:

$$\dot{M}_D = \dot{M}_{fb} - \dot{M}_{prop} - \dot{M}_{acc}, \quad (3)$$

$$\dot{\omega} = \frac{N_{acc} + N_{dip}}{I}. \quad (4)$$

Equation (3) accounts for mass added to the disc through fallback accretion ( $\dot{M}_{fb}$ ) and mass lost from the disc via the propeller mechanism or accretion on to the magnetar ( $\dot{M}_{prop}$  and  $\dot{M}_{acc}$ , respectively). In equation (4),  $I = 0.35MR^2$  is the magnetar's moment of inertia and  $N_{acc}$  and  $N_{dip}$  are the accretion and dipole torques acting on the magnetar, respectively. In this work, we adopt the classical dipole torque experienced by any rotating, magnetized body (Shapiro & Teukolsky 1983).  $N_{acc}$  has two forms dependent on the relationship between  $r_m$  and the magnetar radius,  $R$ . If  $r_m > R$ ,

$$N_{acc} = (GM r_m)^{1/2} (\dot{M}_{acc} - \dot{M}_{prop}), \quad (5)$$

or if  $r_m < R$ ,

$$N_{acc} = (GMR)^{1/2} (\dot{M}_{acc} - \dot{M}_{prop}). \quad (6)$$

In the above equations,  $\dot{M}_{fb}$ ,  $\dot{M}_{prop}$ , and  $\dot{M}_{acc}$  are defined as follows:

$$\dot{M}_{fb} = \frac{M_{fb}}{t_{fb}} \left( \frac{t + t_{fb}}{t_{fb}} \right)^{-5/3}, \quad (7)$$

where  $M_{fb}$  is the available fallback mass and  $t_{fb}$  is the fallback time-scale,

$$\dot{M}_{prop} = \eta_2 \left( \frac{M_D(t)}{t_v} \right), \quad (8)$$

$$\dot{M}_{acc} = (1 - \eta_2) \left( \frac{M_D(t)}{t_v} \right), \quad (9)$$

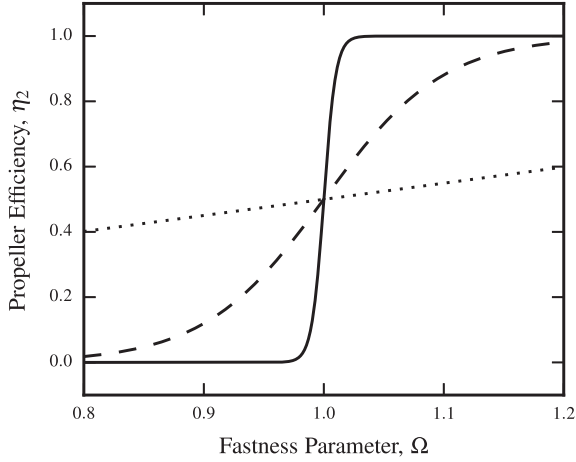


**Figure 1.** A demonstration of how quickly the propeller switches on as a function of  $n$  described by equation (10). The dotted line corresponds to  $n = 1$ , the dashed line corresponds to  $n = 10$  and the solid line corresponds to  $n = 100$ .

where  $\eta_2$  is the efficiency of the propeller mechanism that we define as

$$\eta_2 = \frac{1}{2}(1 + \tanh[n(\Omega - 1)]). \quad (10)$$

This definition of  $\eta_2$  allows accretion to be turned off at a variable rate as the propeller switches on and the combined efficiency of these mechanisms can never exceed 100 per cent. In equation (10),  $\Omega$  is the ‘fastness parameter’,  $\Omega = \omega/(GM_*/r_m^3)^{1/2} = (r_m/r_c)^{3/2}$ , which switches the propeller on as  $\Omega \rightarrow 1$ , and  $n$  controls how ‘sharp’ the propeller switch-on is, as demonstrated in Fig. 1.

We parametrize the available fallback mass as a fraction ( $\delta$ ) of the initial disc mass,  $M_{fb} = \delta M_{D,i}$ , and the fallback time-scale is similarly parametrized as a fraction ( $\epsilon$ ) of the viscous time-scale,  $t_{fb} = \epsilon t_v$ . Equations (3) and (4) are coupled, first order, ordinary differential equations (ODEs) and, using an ODE integrator, the values of  $M_D$  and  $\omega$  can be calculated for a given range of time points. Fig. 2 demonstrates how these fallback parameters affect the disc mass and rotational frequency of a magnetar and disc system and how the propeller condition  $r_m/r_c$  evolves with time.

For short time-scales and small fallback masses ( $\epsilon = 1$ ;  $\delta = 1$ ; solid, red curve), the magnetar spins up more slowly despite rapid fallback because the disc is only being fed small amounts of mass. Hence, the propeller mechanism turns on earlier since the propeller condition is at a lower frequency. For short time-scales and large fallback masses ( $\epsilon = 1$ ;  $\delta = 10$ ; dashed, red curve), mass is quickly added to the disc and the magnetar spins up rapidly. The propeller mechanism is turned on later because the conditional frequency is higher. For long time-scales and small fallback masses ( $\epsilon = 10$ ;  $\delta = 1$ ; solid, green curve), the disc is fed a small amount of mass very slowly and so the magnetar spins up gradually. Again, the propeller condition is at a lower frequency and therefore the mechanism turns on earlier. For long time-scales and large fallback masses ( $\epsilon = 10$ ;  $\delta = 10$ ; dashed, green curve), the disc mass stays constant over a longer period providing a gentle spin-up of the magnetar. Again, the propeller condition is a higher frequency and the mechanism turns on later. Generally speaking, an initially denser disc makes the propeller mechanism harder to initiate, but the magnetar is spun up more rapidly and therefore satisfies the propeller condition at an earlier time.

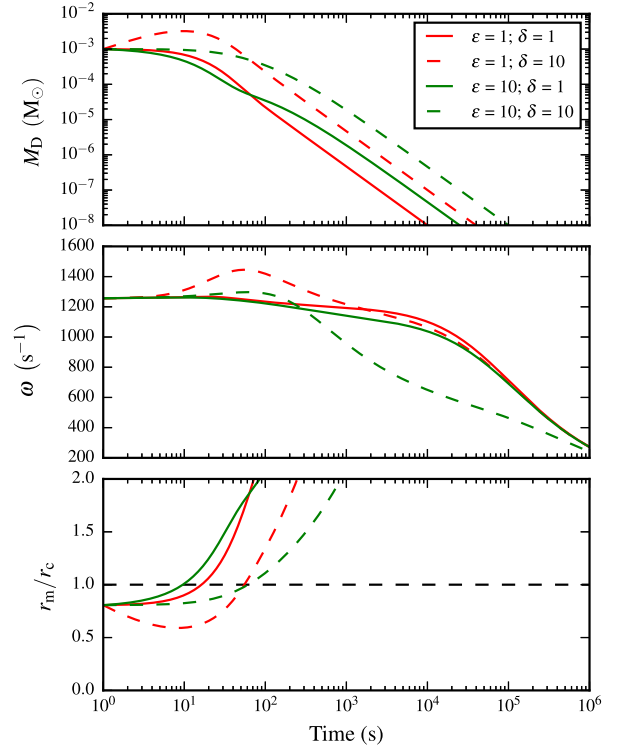


**Figure 2.** A demonstration of how different combinations of the fallback parameters  $\epsilon$  and  $\delta$  affect the disc mass (top panel) and rotation frequency (centre panel) of a magnetar and disc system with fixed magnetic field, initial spin period, initial disc mass and radius. The bottom panel shows the evolution of the propeller condition  $r_m/r_c$  over time for each combination. The system is in the propeller regime when  $r_m/r_c > 1$  (i.e. above the black, dashed line).

Once equations (3) and (4) have been integrated, they are then used to estimate the luminosities from the dipole and propeller components, such that

$$L_{\text{prop}} = \eta_{\text{prop}} \left[ -N_{\text{acc}} \omega - \left( \eta_2 \frac{GM M_D}{r_m t_v} \right) \right] \quad (11)$$

and

$$L_{\text{dip}} = \eta_{\text{dip}} \frac{\mu^2 \omega^4}{6c^3}, \quad (12)$$

where  $\eta_{\text{prop}}$  and  $\eta_{\text{dip}}$  are the propeller and dipole energy–luminosity conversion efficiencies, respectively. The total luminosity is given by the sum of the dipole and propeller luminosities and divided by a beaming fraction to account for the relativistic beaming of the jet:  $L_{\text{tot}} = (1/f_B)(L_{\text{dip}} + L_{\text{prop}})$ .  $1/f_B$  is the fraction of the stellar sphere that is emitting and is related to the half-opening angle of the jet,  $\theta_j$ , as:  $f_B = 1 - \cos(\theta_j)$  (Rhoads 1999; Sari, Piran & Halpern 1999).

## 2.1 Comparing dipole torque equations

For the dipole torque, we have used the classical solution as given by Shapiro & Teukolsky (1983) and Piro & Ott (2011),

$$N_{\text{dip}} = -\frac{\mu^2 \omega^3}{6c^3}. \quad (13)$$

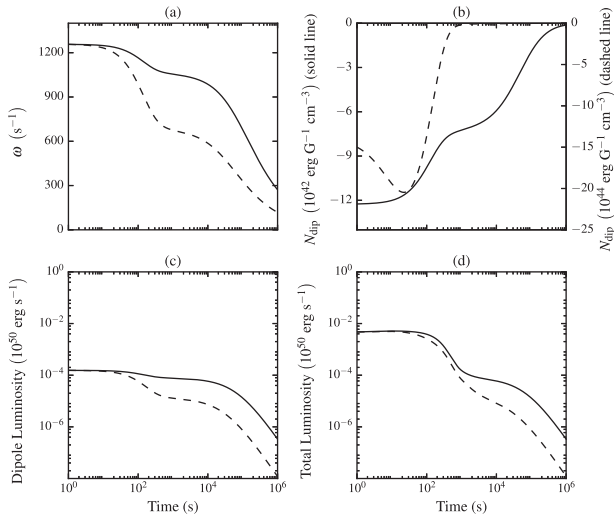


**Figure 3.** A comparison of how equation (13) (solid line; Piro & Ott 2011) and equation (14) (dashed line; Bucciantini et al. 2006) affect (a) the stellar spin; (b) the dipole torque; (c) the dipole luminosity and (d) the total luminosity of a synthetic GRB light curve.

The negative sign indicates that  $N_{\text{dip}}$  spins the magnetar down and produces dipole emission. However, work done by Gompertz et al. (2014) instead uses the following form for the dipole torque:

$$N_{\text{dip}} = -\frac{2}{3} \frac{\mu^2 \omega^3}{c^3} \left( \frac{r_{\text{lc}}}{r_{\text{m}}} \right)^3, \quad (14)$$

which is equation 2 in Bucciantini et al. (2006).

Bucciantini et al. (2006) use a relativistic magnetohydrodynamic (MHD) treatment to solve for the plasma winds emanating from a rotating NS and accretion disc system. They assume that the flow emerges from open flux tubes (providing the extent and shape of the open field line region in the magnetic field is known) and that a truncation of the disc produces more open flux tubes and therefore a greater mass-loss. Equation (14) is then derived from these assumptions. However, it is not certain that these assumptions apply within the model presented in this work and a full MHD treatment of the magnetic propeller is not presented. Therefore, equation (13) is used rather than introducing uncertain assumptions into the model. A comparison between equations (13) and (14) is shown in Fig. 3 using a synthetic GRB light curve with arbitrary parameters.

## 2.2 Exploring parameter space

To determine how the modifications to the propeller model have affected the phenomenological classes outlined in Gompertz et al. (2014, *humped*, *classic*, *sloped* and *stuttering*), the parameter variation experiment they originally performed was repeated with values from Table 1. The magnetar mass and radius were fixed to be  $1.4 M_{\odot}$  and 10 km, respectively, the propeller and dipole efficiencies were set to 100 per cent and the beaming fraction to 1 since they only act to normalize the luminosity here. The produced light curves represented all combinations of  $B$ ,  $P_i$ ,  $M_{\text{D},i}$ ,  $R_{\text{D}}$ ,  $\epsilon$ ,  $\delta$  and  $n$ . The four phenomenological types originally outlined in Gompertz et al. (2014) were recovered and examples of each are shown in Fig. 4. All values for  $n$  appeared commonly in each type suggesting that the model is insensitive to  $n$ .

**Table 1.** Values used to test the effect of parameter variation on the shape of a GRB light curve.  $B$  – magnetic field;  $P_i$  – initial spin period;  $M_{\text{D},i}$  – initial disc mass;  $R_{\text{D}}$  – disc radius;  $\epsilon$  – time-scale ratio;  $\delta$  – fraction of initial disc mass available in the global mass budget;  $n$  – sharpness of propeller switch-on.

$B$	( $10^{15}$ G)	1	5	10	50	–
$P_i$	(ms)	1	5	10	–	–
$M_{\text{D},i}$	( $M_{\odot}$ )	$10^{-5}$	$10^{-4}$	$10^{-3}$	$10^{-2}$	$10^{-1}$
$R_{\text{D}}$	(km)	100	500	1000	–	–
$\epsilon$		1	10	–	–	–
$\delta$		1	10	–	–	–
$n$		1	10	50	–	–

## 2.3 Comparing types to previous work

In order to determine how well the modified model recovered the four types, the parameters given in Table 2 were used to generate light curves using the previous model described in Gompertz et al. (2014). The fallback accretion in the modified model was turned off by setting  $\epsilon = 1$  and  $\delta = 10^{-6}$ , i.e. the amount of fallback mass is so negligible that the magnetar behaves as if only the accretion disc is present and the fallback time-scale becomes irrelevant. The value of  $n$  used was 1 as this is the closest approximation to the propeller switch-on modelled in previous work. Fig. 5 compares the modified model without fallback to the previous work. The difference in dipole luminosity between the two models is explained by our use of the classical dipole torque as discussed in Section 2.1. Equation (13) has a longer dipole duration than equation (14) causing some morphological differences. However, the modified model does not recover the propeller luminosity in all cases, the stuttering type being the most different. Since we have already seen in Fig. 4 that the modified model is capable of reproducing all types successfully, it is suggested that they have moved in parameter space due to the inclusion of  $\dot{M}_{\text{prop}}$  and its link to  $\dot{M}_{\text{acc}}$  through  $\eta_2$ .

## 3 SWIFT SGRBEE SAMPLE

The data for the GRB sample were collected by *Swift*. The *Swift* satellite (Gehrels et al. 2004), launched in 2004, is a multiwavelength observatory dedicated to GRB hunting with rapid slewing capabilities. It carries three instruments: the Burst Alert Telescope (BAT; Barthelmy et al. 2005), the X-ray Telescope (XRT; Burrows et al. 2005) and the Ultra-Violet/Optical Telescope (UVOT; Roming et al. 2005). The *Swift* mission and the UK *Swift* Science Data Centre (UKSSDC;<sup>1</sup> Evans et al. 2007, 2009) provided the data presented in this paper.

The data need to undergo a cosmological  $k$ -correction and absorption correction, as described in Bloom, Frail & Sari (2001), to produce bolometric (1–10 000 keV), redshift-corrected light curves before they can be fitted by the model. This method requires the photon index,  $\Gamma$ , the absorption coefficient,  $\sigma$  (given by the ratio of counts-to-flux unabsorbed to counts-to-flux observed, which are all available on the UKSDCC repository) and the redshift,  $z$ , some of which were found in the literature (see Table 3). For those GRBs with no measured redshift, the sample mean of 0.39 from Gompertz et al. (2014) was used. Alternatively, a randomly generated redshift (e.g. within 1, 2 or even 3 standard deviations of the mean value) could be used. The effect of an increasing  $z$  is an increase in luminosity and earlier on-set times that, as we will see later in this paper,

<sup>1</sup> [www.swift.ac.uk](http://www.swift.ac.uk)

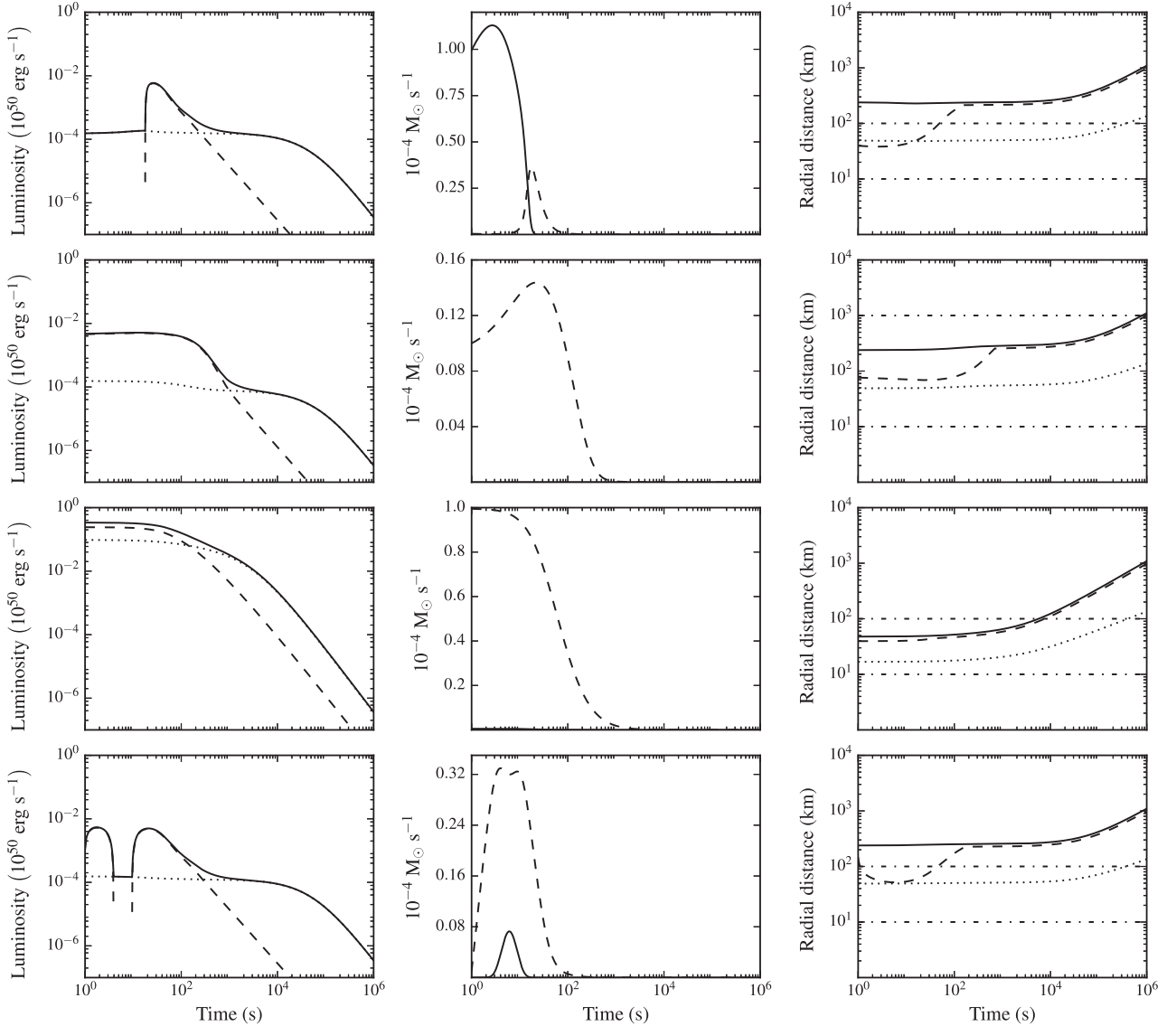


**Figure 4.** Top to bottom: Type I – humped; Type II – Classic; Type III – sloped; Type IV – stuttering. Each row shows plots for one example of each class. They are not fully representative of the range of energetics or morphology for their respective classes since they are intended to highlight the light-curve shapes only. Left-hand panels: synthetic light curves representing the four phenomenological classes. Dotted line – dipole luminosity; dashed line – propeller luminosity; solid line – total luminosity. Centre panels: mass flow rates in the system. Solid line – mass flow rate on to the central magnetar; dashed line – propellered mass flow out of the system. Right-hand panels: positions of key radii relative to the centre of the magnetar. Dashed line – Alfvén radius; dotted line – co-rotation radius; solid line – light cylinder radius. Lower horizontal dot-dashed line is the magnetar radius, upper horizontal dot-dashed line is the outer disc radius,  $R_D$ .

**Table 2.** Main parameters used to compare light curves from the previous model (Gompertz et al. 2014) with the modified model without fallback accretion.

		Humped	Classic	Sloped	Stuttering
$B$	( $10^{15}$ G)	1	1	10	5
$P_1$	(ms)	5	5	5	5
$M_{D,i}$	( $M_\odot$ )	$10^{-3}$	$10^{-4}$	$10^{-4}$	$10^{-2}$
$R_D$	(km)	100	1000	1000	500

causes the model to favour larger initial disc masses and fallback mass budgets. Since these may not have a physical basis, we have chosen to use the sample mean, as in previous work by Gompertz et al. (2014).

The sample studied in Gompertz et al. (2013, 2014) has been expanded here by selecting identified SGRBEEs from Kaneko et al. (2015, which covers bursts to the end of 2012) that have good data available in the *Swift* archive. Plus GRBs 150424A and 160410A which are identified as EE bursts within GCN Circulars (Norris et al. 2015; Sakamoto et al. 2016, respectively). The data used in the fitting incorporates XRT data and BAT data that have been extrapolated into the XRT bandpass (available from the UKSDCC Burst Analyser tool) since the effect of the EE is not always evident in the XRT light curve alone.

#### 4 FITTING ROUTINE

A Markov chain Monte Carlo simulation (MCMC; MacKay 2003, chap. 4) was used to fit the model to data as there are a minimum



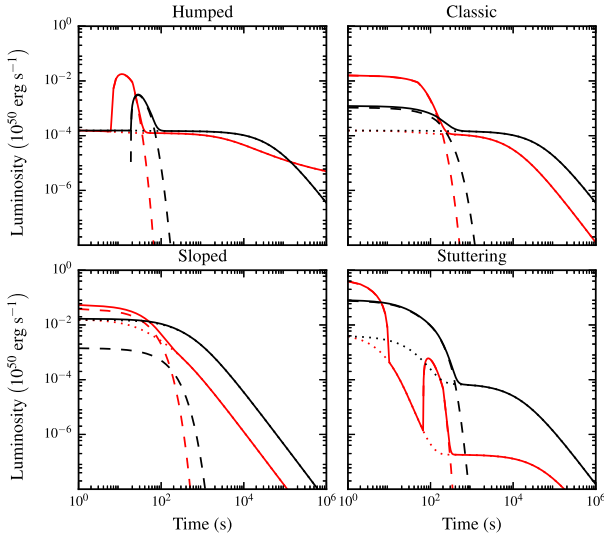


**Figure 5.** Comparison of light curves generated by the previous model (Gompertz et al. 2014; red curves) and the modified model without fallback accretion (black curves). The fallback was turned off by setting  $\epsilon = 1$  and  $\delta = 10^{-6}$ ;  $n = 1$  as the closest approximation to the switch on in the previous model. Solid lines – total luminosity; dashed lines – propeller luminosity; dotted lines – dipole luminosity.

**Table 3.** The sample of SGRBEEs and the parameters required for a cosmological  $k$ -correction. For GRBs with an unknown redshift (marked with an \*), the sample mean of 0.39 from Gompertz et al. (2014) was used. <sup>†</sup>Upper limit (D’Avanzo et al. 2009). <sup>a</sup>Prochaska et al. (2005); <sup>b</sup>Soderberg, Berger & Ofek (2005); <sup>c</sup>Price, Berger & Fox (2006); <sup>e</sup>Berger (2007); <sup>d</sup>Cenko et al. (2006); <sup>e</sup>Graham et al. (2009); <sup>f</sup>D’Avanzo et al. (2007); <sup>g</sup>Selsing et al. (2016).

GRB	$\Gamma$	$\sigma$	$z$
050724	$1.58^{+0.21}_{-0.19}$	1.26	0.2578 <sup>a</sup>
051016B	$1.85^{+0.14}_{-0.13}$	1.31	0.9364 <sup>b</sup>
051227	$2.1^{+0.4}_{-0.4}$	1.31	2.8 <sup>†</sup>
060614	$1.78^{+0.08}_{-0.08}$	1.06	0.1254 <sup>c</sup>
061006	$2.1^{+0.6}_{-0.4}$	1.61	0.4377 <sup>c</sup>
061210	$2.60^{+1.92}_{-0.71}$	3.48	0.4095 <sup>d</sup>
070714B	$1.79^{+0.24}_{-0.22}$	1.15	0.9224 <sup>e</sup>
071227	$1.5^{+0.6}_{-0.5}$	1.02	0.381 <sup>f</sup>
080123	$2.46^{+1.04}_{-0.70}$	1.71	0.39*
080503	$2.38^{+0.42}_{-0.16}$	1.24	0.39*
100212A	$1.90^{+0.40}_{-0.18}$	1.37	0.39*
100522A	$2.40^{+0.17}_{-0.16}$	2.45	0.39*
111121A	$1.78^{+0.21}_{-0.20}$	1.42	0.39*
150424A	$1.98^{+0.24}_{-0.22}$	1.23	0.39*
160410A	$1.5^{+0.7}_{-0.6}$	1.02	1.717 <sup>g</sup>

of six parameters and the MCMC will efficiently search a large portion of parameter space and increase the probability of finding the global minimum of the model. However, the MCMC method requires a burn-in phase that is loosely defined as an unknown number of steps at the beginning of the simulation where each ‘walker’ attempts to find the lowest area of probability space. The chain is generally considered to be burned in when all walkers have converged on to this area of probability space. The ‘EMCEE’ module was used to handle the MCMC (Foreman-Mackey et al. 2013).

**Table 4.** Upper and lower limits placed on the fitting parameters in the MCMC.  $M_{D,i}$ ,  $R_D$ ,  $\epsilon$  and  $\delta$  were searched in log-space for efficiency.

		Lower	Upper
$B$	( $10^{15}$ G)	$10^{-3}$	10
$P_i$	(ms)	0.69	10
$M_{D,i}$	( $M_\odot$ )	$10^{-3}$	$10^{-1}$
$R_D$	(km)	50	2000
$\epsilon$		0.1	1000
$\delta$		$10^{-5}$	50
$\eta_{\text{dip}}$	(per cent)	1	100
$\eta_{\text{prop}}$	(per cent)	1	100
$1/f_B$		1	600

To construct the posterior probability distribution, a Gaussian log-likelihood function of the following form was chosen

$$\ln(p_{\text{likelihood}}) = -\frac{1}{2} \sum_{i=1}^N \left( \frac{y_i - \hat{y}_i}{\sigma_i} \right)^2, \quad (15)$$

where  $y_i$  is a data point,  $\sigma_i$  is its associated uncertainty and  $\hat{y}_i$  is a model point calculated at the same  $x$ -value as  $y_i$ . The *Swift* light curves used here are binned to contain a minimum of 20 photons per time bin (an exception may be applicable in the last bin) making Gaussian statistics suitable. A prior probability that is flat when the parameters are within the limits given in Table 4 was also chosen,

$$\ln(p_{\text{prior}}) = \begin{cases} 0 & x_l < x < x_u \\ -\infty & \text{otherwise.} \end{cases} \quad (16)$$

Hence, the full posterior probability distribution is given by

$$\ln(p) = \ln(p_{\text{likelihood}}) + \ln(p_{\text{prior}}). \quad (17)$$

For the MCMC, 100 affine invariant walkers (Goodman & Weare 2010) were used and ran for a 50 000 step burn-in phase to allow the walkers to test all of parameter space. After this run, the best 100 distinct probabilities were chosen to serve as the starting point for the final MCMC run of the same length. This made sure that the parameters recovered were representative of the global minimum, not a local minimum, and reduces the burn-in of the chain to  $\lesssim 1000$  steps in most cases. Although, if the time series (parameter or probability value versus model number for each walker) showed that the chain had not fully converged, the process of selecting the 100 best probabilities was repeated and the chain run again until convergence was achieved. The optimal parameters were found by taking the median of the posterior probability distributions and their uncertainties are given by the 95 per cent percentiles. We chose the median, rather than the mean or mode, since it is less sensitive to the tails of distributions and is preserved under reversible transformations of the data (e.g.  $\log_{10} \epsilon \rightarrow \epsilon$ ). Fits for the SGRBEE sample were produced with a range of free parameters ( $p$ ):  $p = 6$  ( $B$ ,  $P_i$ ,  $M_{D,i}$ ,  $R_D$ ,  $\epsilon$  and  $\delta$ ); 7 (original 6 plus  $1/f_B$ ); 8 (original 6 plus  $\eta_{\text{dip}}$  and  $\eta_{\text{prop}}$ ) and 9 (all listed parameters).  $\eta_{\text{dip}}$ ,  $\eta_{\text{prop}}$  and  $1/f_B$  were fixed to 5 per cent, 40 per cent and 1 per cent, respectively, when they were not free parameters, in keeping with Gompertz et al. (2014). The fits were repeated for fixed values of  $n = 1, 10, 100$  and the corrected Akaike Information Criterion (AICc; Cavanaugh & Neath 2011) was used to establish the best-fitting models. We chose this statistic since it allows us to compare models of varying free parameter number ( $p$ ).

AICc is given by the following equation

$$\text{AICc} = -2 \ln(L) + 2k + \frac{2k(k+1)}{N-k-1}, \quad (18)$$

**Table 5.** AICc values for models using 6, 7, 8 and 9 free parameters ( $p$ ) for  $n = 1, 10, 100$ . Underlined values are the lowest AICc values for each  $n$  bracket and values in bold are the minima across all values of  $n$ . Values marked with an \* are modified since  $N - k - 1 = 0$  for these models.

GRB	$n = 1$				$n = 10$				$n = 100$			
	$p = 6$	$p = 7$	$p = 8$	$p = 9$	$p = 6$	$p = 7$	$p = 8$	$p = 9$	$p = 6$	$p = 7$	$p = 8$	$p = 9$
050724	2415	1790	1975	<u>1682</u>	2496	2216	2005	<b>1507</b>	2509	2128	2007	<u>1610</u>
051016B	802	540	771	<u>531</u>	785	562	742	<u>518</u>	785	549	742	<b>435</b>
051227	538	267	318	<u>235</u>	535	271	317	<u>235</u>	535	381	317	<b>233</b>
060614	47 390	47 256	47 521	<b>44 709</b>	48 428	47 275	46 950	<u>44 746</u>	48 422	47 263	48 013	<u>45 278</u>
061006	269	<u>244</u>	252	250	317	<b>242</b>	543	253	323	<u>244</u>	262	257
061210	<u>673</u>	802	1054*	103 101	677	<b>149</b>	1649*	5148	670	<u>210</u>	969*	5127
070714B	1303	1419	<u>1260</u>	1352	1302	1397	<u>1260</u>	1301	1302	1844	1260	<b>1180</b>
071227	335	161	163	<b>158</b>	226	339	<u>161</u>	163	225	265	<u>161</u>	230
080123	308	308	<u>298</u>	305	337	<u>291</u>	308	307	360	<b>283</b>	330	360
080503	<u>2335</u>	2375	2474	2474	2375	2379	<b>2294</b>	2583	2927	<u>2475</u>	3539	2784
100212A	9055	8372	8130	<b>7310</b>	9299	8271	8988	<u>8196</u>	9258	<u>8498</u>	8988	8588
100522A	29 377	<u>22 992</u>	27 472	23 419	27666	23326	26 116	<b>22 184</b>	27 531	22 460	26 744	<u>22 411</u>
111121A	1754	<u>1747</u>	1761	1803	1753	1751	<u>1748</u>	1766	1753	1750	1761	<b>1742</b>
150424A	2377	2997	2223	<b>1334</b>	2315	51 246	<u>2170</u>	58 080	2315	1795	2171	<u>1432</u>
160410A	974	<u>473</u>	546	18742	1115	<u>366</u>	546	403	1255	412	546	<b>359</b>

where  $k$  is the number of free parameters and  $N$  is the number of observations in the data set. This penalizes a model for ‘overfitting’ and scales with  $k$ . We have substituted equation (15) for the maximum log-likelihood  $\ln(L)$ , which then cancels down to the  $\chi^2$  statistic. The minimum AICc value within a set is then representative of the optimum model fit since if the AICc value of a model that has a large number of free parameters (and hence a large penalty) is less than a model with fewer free parameters (and hence a small penalty), then it can be generally assumed that the extra parameters improve the quality of fit.

## 5 RESULTS AND DISCUSSION

Table 5 presents the AICc values for all results of the fitting routine. The large spread of values is representative of the difficulty  $\chi^2$  (the root of the AICc) has comparing a smooth model with highly variable data, especially in the early-time BAT data. Table 5 shows that the general picture of the model is stable over all  $n$  values since there is a reasonable spread of best fits. This also confirms the observation made in Section 2.2 that the model is reasonably insensitive to  $n$ . Increasing  $n$  only makes features such as humps appear sharper, which does not have a great impact on the overall quality of the fit. The best global fits to the SGRBEE sample (bold values in Table 5) are presented in Fig. 6.

The  $p = 6$  set represents the core physics of the model by constraining the fundamental properties of the magnetar ( $B$  and  $P_i$ ), the accretion disc ( $M_{D,i}$  and  $R_D$ ) and the fallback ( $M_{fb}$  and  $t_{fb}$  through  $\delta$  and  $\epsilon$ , respectively) and is the most energetically restricted case compared to the  $p = 9$  case that has the largest energy reservoir. Furthermore,  $\eta_{dip}$  and  $\eta_{prop}$  determine the efficiency at which the dipole and propeller mechanisms, respectively, need to work in order to convert the energy to luminosity. Lastly,  $f_B$  accounts the anisotropy of the radiation ( $1/f_B$  is the solid angle of emission). The results of the MCMC were analysed for parameter correlations though none were found since our method of selecting the best probabilities after the burn-in phase removes any correlation by placing the parameters in the global minimum.

The  $k$ -correction performed in Section 3 assumes isotropic emission, whereas in actuality, GRBs are beamed into a very narrow opening angle due to their relativistic velocity (Fruchter et al. 1999; Harrison et al. 1999; Frail et al. 2001). Rather than divide the data

down to a beam-corrected level, our routine works to multiply the model up to the isotropic luminosity level so that model comparison becomes easier on the same scale. The morphologies of the fits change as each new parameter is introduced since they handle the high luminosities at early times allowing the core parameters to reconfigure. This means that there can be more energy available at late times to fit the fading afterglow.

It is interesting to compare the freedom of the model (i.e. how many free parameters are used) with the ‘sharpness’ of the propeller (i.e. the  $n$  value). Generally speaking, the AICc value of the fit improves as the number of free parameters increases, whereas, increasing  $n$  for the same number of free parameters often does not improve the fit. Also,  $p = 8$  fits often perform worse than  $p = 7$  fits implying that the beaming fraction has a greater role within the model than the efficiencies, but the inclusion of all three of these parameters are most preferable. Table 6 shows a comparison of the jet half-opening angles derived from the best fits in this work with hydrodynamical modelling performed by Ryan et al. (2015) for four GRBs common to both studies. Our model produces systematically narrower jets (most likely caused by the model attempts to fit the early-time luminosity) that are partially consistent with Ryan et al. (2015) in errors (e.g. GRBs 051016B and 060614), and where they are not (e.g. GRB 061006), they are broadly consistent to  $\sim 2\sigma$ – $2.5\sigma$ .

Comparing our results with that of Gompertz et al. (2014), we can see the inclusion of fallback accretion within the propeller model allows for an improvement in fitting the ‘tail’ of the fading afterglow. This can be seen in GRBs 051227, 060614 and 061006, where Gompertz et al. (2014) did not produce such good fits to the tail. Hence, fallback accretion is a necessary addition to the propeller model in order to fully explain the energetics and morphologies of SGRBEEs. Additionally, the extended model handles variability and flares within the data much more naturally than Gompertz et al. (2014) and copes with the early-time luminosity detected by BAT.

The parameters derived from the fits in Fig. 6 are presented in Table 7. We find that the magnetic fields derived from the fits are in the moderate to high end of the parameter space and that the sample generally has slow initial spins. The slow initial spins are most likely due to the additional fallback spinning the magnetar up and, therefore, the constraints on high initial spin rates is relaxed. This has an impact on the value of the magnetic field derived as

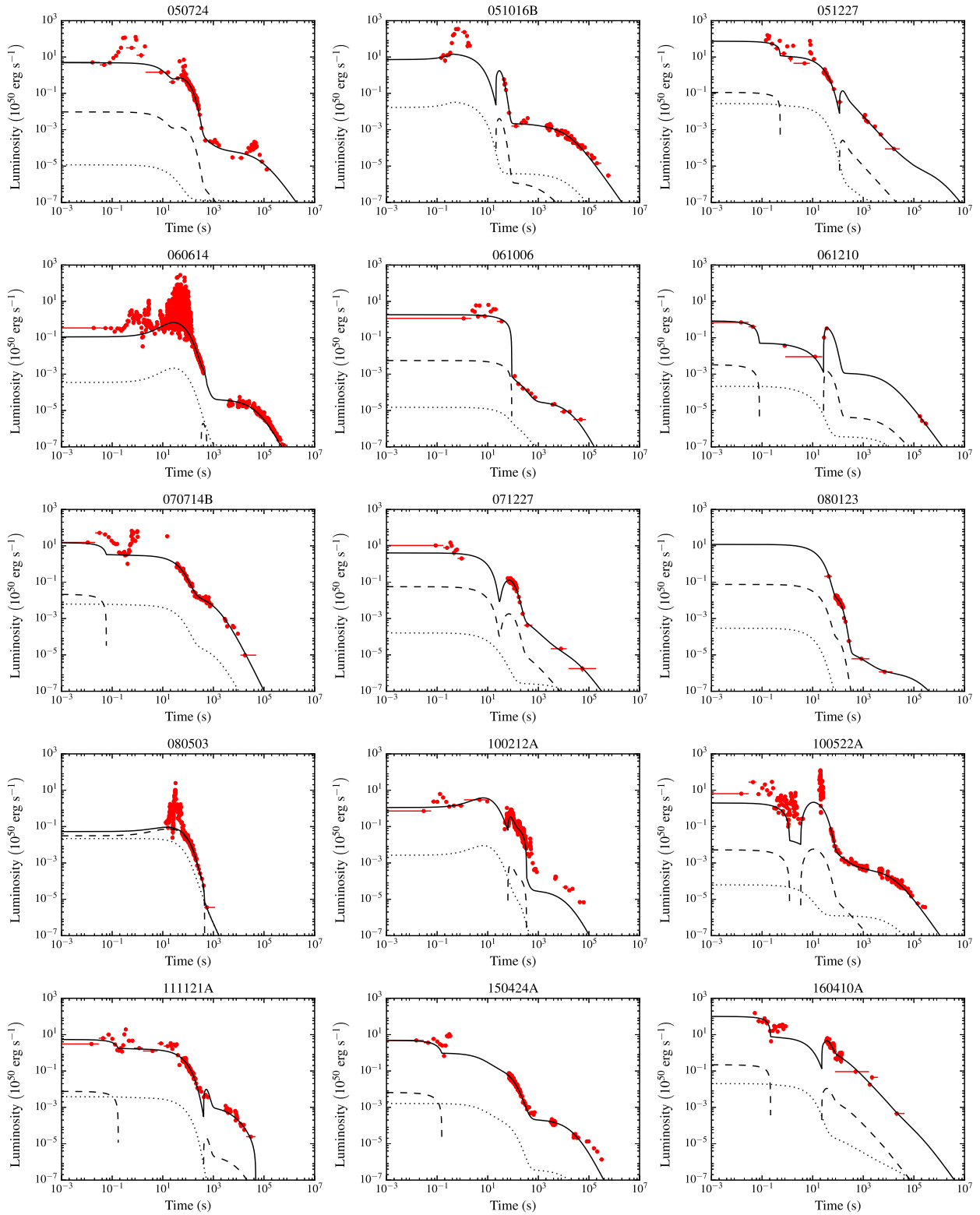


**Figure 6.** Best global fits to the SGRBEE sample (bold values in Table 5). Dashed line – propeller luminosity; dotted line – dipole luminosity; solid line – total luminosity; red points – combined BAT and XRT data.



**Table 6.** Table showing the half-opening angles (in radians) for four GRBs, calculated from  $f_B = 1 - \cos(\theta_j)$ .  $\theta_j$  values are from the global best fits of this work (uncertainties are 95 per cent confidence interval);  $\theta_0$  values are from Ryan et al. (2015).

GRB	$\theta_j$	$\theta_0$
051016B	$0.07^{+0.11}_{-0.11}$	$0.35^{+0.11}_{-0.24}$
060614	$0.079^{+0.359}_{-0.500}$	$0.293^{+0.122}_{-0.085}$
061006	$0.078^{+0.088}_{-0.081}$	$0.407^{+0.068}_{-0.173}$
070714B	$0.06^{+0.18}_{-0.12}$	$0.33^{+0.11}_{-0.11}$

the fit moves along the correlation between  $B$  and  $P_i$  discussed in Gompertz et al. (2014). The sample fits also tend to favour massive discs and narrow jet opening angles. This is most likely due to the model extracting as much of the available energy as possible to fit the high luminosities at early times in the light curve, data which was not included in the fits of Gompertz et al. (2014). The values of  $\epsilon$ ,  $\delta$ ,  $\eta_{\text{dip}}$  and  $\eta_{\text{prop}}$  are widely distributed throughout the parameter space. The derived parameters are consistent with predictions for a magnetar (Giacomazzo & Perna 2013; Mereghetti, Pons & Melatos 2015; Rea et al. 2015) and are also consistent with the results in Gompertz et al. (2014).

We will now examine how increasing the number of free parameters affects the fits in three GRBs from the sample. GRB 060614 has been chosen since this is a uniquely interesting burst given its characteristics. GRBs 050724 and 111121A were chosen as examples of the model behaving consistently well, or vice versa, over the different parameter sets.

## 5.1 GRB 050724

Fig. 7 shows a comparison of fits with varying  $p$  to GRB 050724 for  $n = 100$ . For  $p = 6$ , the model does a reasonable job of fitting the high

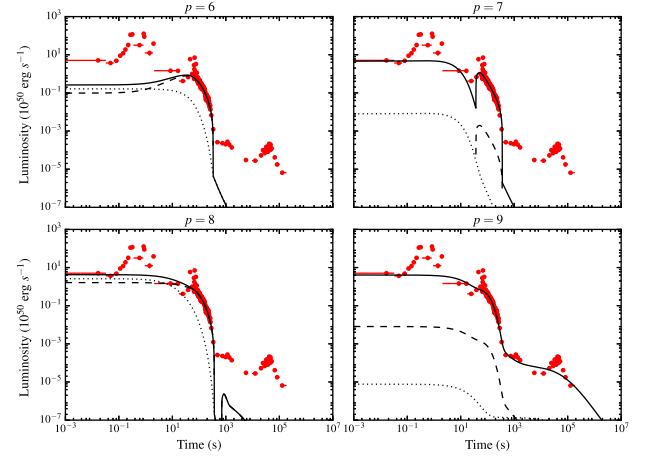


**Figure 7.** Models fitted to GRB 050724 with  $n = 100$  and  $p = 6$  (top left), 7 (top right), 8 (bottom left) and 9 (bottom right). Solid line – total luminosity; dashed line – propeller luminosity; dotted line – dipole luminosity; red points – combined BAT and XRT data.

luminosity at early times but does not retain enough energy to fit the tail. The fit demanded a large amount of fallback,  $\delta = 1.65^{+1.26}_{-0.62}$ , on a short time-scale,  $\epsilon = 0.13^{+0.04}_{-0.02}$ , and a very rapid spin period,  $P = 0.69$  ms (limit), in order to reach such a high luminosity so soon. Since the fallback mass reaches the disc quickly, there is nothing left in the fallback budget to provide energy for the late-time emission.  $p = 7$  and 8 provide improved fits to the early-time luminosity but again fail to fit the fading tail despite the additional parameters being pushed to the higher end of their limits, e.g.  $1/f_B = 578^{+21}_{-71}$  for  $p = 7$  and  $\eta_{\text{prop}} = 99^{+1}_{-5}$  per cent for  $p = 8$  ( $\eta_{\text{dip}} = 12^{+2}_{-2}$  per cent).  $p = 9$  is the only model that succeeds in fitting the tail but still requires a highly efficient emission mechanism for the propeller,  $\eta_{\text{prop}} = 86^{+13}_{-18}$  per cent, and a very narrow beaming angle,  $1/f_B = 502^{+93}_{-103}$ .

**Table 7.** Parameters derived from the best global fits to the SGRBEE sample (bold values in Table 5). Reported errors are 95 per cent. Values marked with an [L] have reached a parameter limit; those marked with [F] were fixed during fitting. The  $\chi^2_{\text{red}}$  values are also presented to indicate goodness of fit.

GRB	$n$ [F]	$B$ ( $\times 10^{15}$ G)	$P_i$ (ms)	$M_{D,i}$ ( $\times 10^{-2} M_\odot$ )	$R_D$ (km)	$\epsilon$	$\delta$	$\eta_{\text{dip}}$ (per cent)	$\eta_{\text{prop}}$ (per cent)	$1/f_B$	$\chi^2_{\text{red}}$
050724	10	$4.81^{+0.11}_{-0.23}$	$9.70^{+0.29}_{-0.92}$	$0.489^{+0.070}_{-0.023}$	$320^{+5}_{-5}$	$1.26^{+11.87}_{-1.15}$	$(0.50^{+1.82}_{-0.30}) \times 10^{-3}$	$5^{+1}_{-1}$	$86^{+13}_{-18}$	$508^{+87}_{-100}$	6
051016B	100	$9.95^{+0.05}_{-0.12}$	$3.44^{+0.19}_{-0.17}$	$9.84^{+0.16}_{-0.67}$	$54^{+4}_{-2}$	$262.25^{+443.06}_{-244.97}$	$(0.39^{+1.33}_{-0.28}) \times 10^{-4}$	$25^{+22}_{-7}$	$77^{+21}_{-31}$	$431^{+158}_{-175}$	5
051227	100	$5.15^{+0.72}_{-0.54}$	$3.02^{+0.29}_{-0.31}$	$9.31^{+0.66}_{-1.32}$	$263^{+10}_{-16}$	$0.94^{+22.57}_{-0.83}$	$(1.28^{+4.78}_{-0.97}) \times 10^{-2}$	$89^{+10}_{-25}$	$52^{+27}_{-17}$	$526^{+71}_{-149}$	7
060614	1	$6.02^{+0.05}_{-0.05}$	$9.99^{+0.01}_{-0.04}$	$9.99^{+0.01}_{-0.05}$	$680^{+6}_{-6}$	$998.58^{+1.37}_{-6.15}$	$2.29^{+0.05}_{-0.05}$	$99^{+1}_{-4}$	1[L]	$322^{+16}_{-8}$	19
061006	10	$2.60^{+0.53}_{-0.35}$	$6.83^{+1.88}_{-4.20}$	$1.14^{+3.82}_{-0.37}$	$1915^{+82}_{-344}$	$131.21^{+92.86}_{-51.42}$	$17.78^{+6.58}_{-4.30}$	5[F]	40[F]	$330^{+258}_{-304}$	15
061210	10	$7.60^{+0.45}_{-0.40}$	$6.00^{+0.68}_{-0.59}$	$1.71^{+0.26}_{-0.23}$	$124^{+3}_{-3}$	$733.05^{+250.59}_{-285.29}$	$(9.41^{+4.70}_{-3.92}) \times 10^{-3}$	5[F]	40[F]	$241^{+74}_{-55}$	23
070714B	100	$6.58^{+1.56}_{-1.74}$	$4.91^{+0.80}_{-1.15}$	$9.32^{+0.65}_{-1.47}$	$463^{+20}_{-19}$	$30.93^{+3.52}_{-3.43}$	$1.68^{+0.12}_{-0.12}$	$87^{+12}_{-34}$	$80^{+19}_{-19}$	$536^{+62}_{-129}$	11
071227	1	$8.59^{+1.35}_{-2.89}$	$5.99^{+2.30}_{-3.34}$	$1.54^{+3.03}_{-0.62}$	$268^{+22}_{-21}$	$9.60^{+50.17}_{-9.47}$	$(1.35^{+5.10}_{-0.75}) \times 10^{-3}$	$3^{+4}_{-2}$	$59^{+39}_{-41}$	$72^{+197}_{-59}$	4
080123	100	$9.55^{+0.43}_{-1.06}$	$6.21^{+1.22}_{-1.41}$	$0.928^{+0.374}_{-0.190}$	$231^{+7}_{-6}$	$26.21^{+52.13}_{-24.42}$	$(5.97^{+6.81}_{-2.04}) \times 10^{-5}$	5[F]	40[F]	$158^{+41}_{-60}$	6
080503	10	$1.97^{+0.45}_{-0.32}$	$1.85^{+0.59}_{-0.55}$	$0.33^{+1.08}_{-0.22}$	$566^{+65}_{-36}$	$0.42^{+0.21}_{-0.20}$	$10.35^{+25.85}_{-8.28}$	$70^{+29}_{-48}$	$29^{+27}_{-15}$	1[F]	9
100212A	1	$9.97^{+0.03}_{-0.13}$	$7.26^{+0.23}_{-0.23}$	$9.91^{+0.08}_{-0.33}$	$163^{+1}_{-1}$	$978.19^{+21.03}_{-94.38}$	$(7.12^{+0.36}_{-0.68}) \times 10^{-1}$	$77^{+22}_{-22}$	$17^{+5}_{-5}$	$422^{+166}_{-99}$	19
100522A	10	$9.32^{+0.05}_{-0.09}$	$9.95^{+0.04}_{-0.19}$	$0.467^{+0.012}_{-0.003}$	$75^{+1}_{-1}$	$5.44^{+3.14}_{-2.50}$	$(8.76^{+2.39}_{-1.20}) \times 10^{-4}$	$7^{+3}_{-3}$	$73^{+26}_{-26}$	$375^{+205}_{-99}$	89
111121A	100	$4.19^{+0.32}_{-0.28}$	$4.38^{+0.64}_{-0.46}$	$8.61^{+1.31}_{-1.44}$	$812^{+12}_{-12}$	$99.59^{+30.58}_{-23.43}$	$(2.84^{+0.36}_{-0.33}) \times 10^{-3}$	$84^{+16}_{-32}$	$41^{+12}_{-13}$	$474^{+120}_{-180}$	13
150424A	1	$9.80^{+0.19}_{-0.73}$	$5.74^{+0.13}_{-0.41}$	$9.94^{+0.06}_{-0.22}$	$826^{+19}_{-22}$	$339.09^{+61.77}_{-53.67}$	$6.92^{+0.81}_{-0.78}$	$19^{+1}_{-2}$	$99^{+4}_{-4}$	$594^{+6}_{-22}$	11
160410A	100	$5.02^{+0.81}_{-0.82}$	$2.33^{+0.78}_{-0.65}$	$6.23^{+3.36}_{-2.03}$	$95^{+6}_{-7}$	$12.25^{+10.49}_{-7.56}$	$(2.20^{+0.63}_{-0.47}) \times 10^{-2}$	$24^{+20}_{-15}$	$78^{+21}_{-39}$	$419^{+172}_{-223}$	6

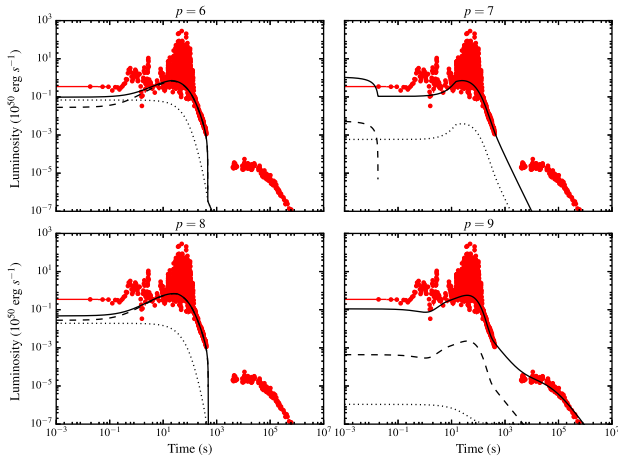


**Figure 8.** Models fitted to GRB 060614 with  $n = 100$  and  $p = 6$  (top left), 7 (top right), 8 (bottom left) and 9 (bottom right). Solid line – total luminosity; dashed line – propeller luminosity; dotted line – dipole luminosity; red points – combined BAT and XRT data.

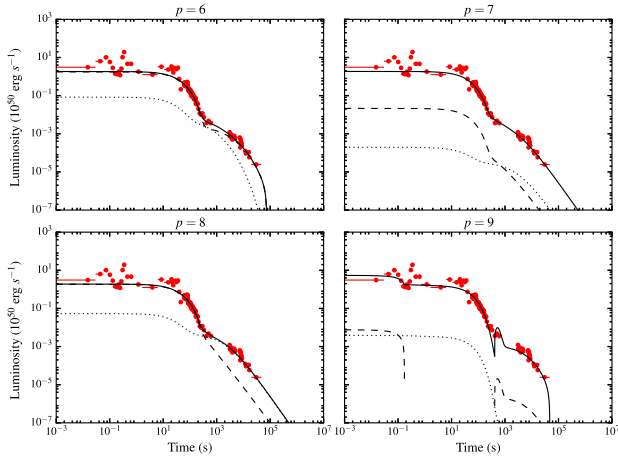


**Figure 9.** Models fitted to GRB 11121A with  $n = 100$  and  $p = 6$  (top left), 7 (top right), 8 (bottom left) and 9 (bottom right). Solid line – total luminosity; dashed line – propeller luminosity; dotted line – dipole luminosity; red points – combined BAT and XRT data.

It is interesting to note the late-time giant flare within the tail of GRB 050724 that the model has not been able to fit. At present, the phenomena that cause such large outbursts at these late times are still poorly understood (see Falcone et al. 2006; Curran et al. 2008; Chincarini et al. 2010).

## 5.2 GRB 060614

GRB 060614 poses a challenge to typical long/short classification scheme since it has a duration of  $\sim 100$  s but the hard spectrum and lack of supernova connection are more indicative of the short classification (Mangano et al. 2007; Zhang et al. 2007; Xu et al. 2009).

Fig. 8 presents model fits of varying  $p$  and  $n = 100$  to data for GRB 060614.  $p = 6$  provides a good fit to the early-time luminosity but after  $\sim 100$  s, its energy reservoir is depleted and the light curve rapidly drops off before fitting the tail. This demands a rapid spin period,  $P = 0.90^{+0.01}_{-0.01}$  ms, and a large amount of fallback mass,  $\delta = 49.61^{+0.38}_{-1.63}$ , reaching the disc on a short time-scale,

**Table 8.** AICc values for fits to the SGRBEE sample with varying  $p$  values and  $n = 1$  with data  $< 10$  s excluded. Values in bold face are the minimum value for each GRB. \*GRB 061210 has fewer data points than free parameters resulting in a negative AICc value that was not considered when choosing the best fit.

GRB	$p = 6$	$p = 7$	$p = 8$	$p = 9$
050724	1611	1489	1561	<b>1259</b>
051016B	340	252	310	<b>153</b>
051227	178	<b>53</b>	59	70
060614	48 086	43 738	43 728	<b>43 610</b>
061006	177	<b>90</b>	114	123
061210	−17*	181	<b>66</b>	357
070714B	203	215	<b>177</b>	195
071227	112	<b>89</b>	100	101
080123	354	308	<b>298</b>	319
080503	2281	2375	<b>2157</b>	2339
100212A	8198	7602	7771	<b>7073</b>
100522A	8530	7401	7725	<b>6322</b>
111121A	872	<b>782</b>	819	787
150424A	366	279	354	<b>251</b>
160410A	495	<b>149</b>	212	222

$\epsilon = 0.31^{+0.03}_{-0.03}$ .  $p = 7$  adds more structure to the early-time luminosity and has a more gradual decrease of emission but still fails to reach the tail, whereas,  $p = 8$  is very much a repeat of  $p = 6$  and offers no improvement. Again,  $p = 9$  offers the best results for fitting to the tail but requires a very efficient emission mechanism for the propeller,  $\eta_{\text{prop}} = 100$  per cent (limit), and a moderate beaming fraction,  $1/f_B = 251^{+6}_{-7}$ . Oddly, this model requires the least efficient dipole emission as well,  $\eta_{\text{dip}} = 1$  per cent (limit). This is probably due to the difference in EE and dipole luminosity being the greatest in GRB 060614 and so the model has to do something to achieve a drop in luminosity spanning several orders of magnitude while maintaining parameters that can produce bright, early emission.

GRB 060614 continues to be a very odd case when we examine its best-fitting parameters in Table 7 relating to the fit in Fig. 6 and  $n = 10$ . It is one of the slowest rotating candidates with one of the most massive and most slowly fed discs. Also, the dipole and propeller emission efficiencies have completely reversed roles with  $\eta_{\text{dip}} = 99^{+1}_{-4}$  per cent and  $\eta_{\text{prop}} = 1$  per cent (limit). The propeller's main job is to modulate the spin in order to achieve the desired luminosities. Since the propeller plays no role in this particular fit, this indicates that that has been completely taken over by the fallback.

## 5.3 GRB 11121A

Fig. 9 presents model fits of varying  $p$  and  $n = 100$  to data for GRB 11121A. This is an example of the model behaving well across all values of  $p$ . Despite the fits for  $p = 6, 7$  and  $8$  looking very similar, the parameters derived from the fits vary quite significantly. For  $p = 6$  and  $8$ , relatively small values of magnetic field are recovered,  $B = (2.00^{+0.12}_{-0.11}) \times 10^{15}$  G and  $B = (1.53^{+1.40}_{-0.31}) \times 10^{15}$  G, respectively, whereas  $p = 7$  has a large magnetic field of  $B = (8.15^{+1.77}_{-4.65}) \times 10^{15}$  G. The initial spin values for these fits also follow a similar pattern with spins near the break-up limit for  $p = 6$  and  $8$ ,  $P_i = 0.69$  ms (limit) and  $P_i = 0.89^{+0.16}_{-0.17}$  ms, respectively, and a much slower spin for  $p = 7$ ,  $P_i = 6.36^{+1.96}_{-3.76}$  ms.

Lastly, the  $p = 9$  fit has derived parameters in the moderate region of parameter space,  $B = (4.19^{+0.32}_{-0.28}) \times 10^{15}$  G and

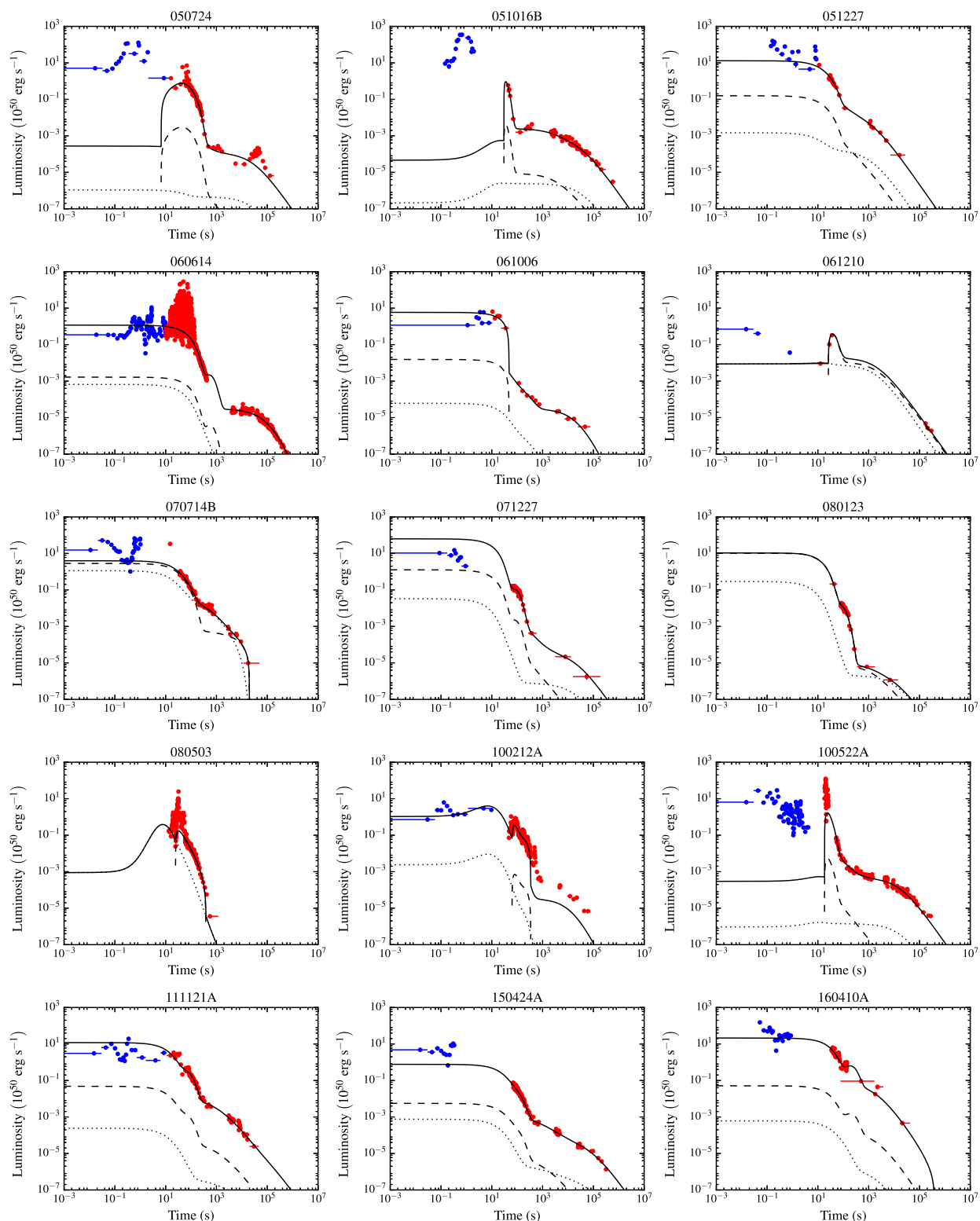


**Figure 10.** Global best-fitting models produced from fitting to the SGRBEE sample for  $n = 1$  and excluding data  $< 10$  s (bold values in Table 8). Solid, black line – total luminosity; dashed, black line – propeller luminosity; dotted, black line – dipole luminosity. Points are combined BAT and XRT data: red points have been included in the fitting, blue points were excluded.

$P_1 = 4.38^{+0.64}_{-0.46}$  ms. It has a slowly fed disc with a small amount of fallback mass,  $\epsilon = 99.59^{+30.58}_{-23.43}$  and  $\delta = (2.84^{+0.36}_{-0.33}) \times 10^{-3}$ . We derive a propeller efficiency consistent with the value used to Gompertz et al. (2014) of  $\eta_{\text{prop}} = 41.48^{+11.99}_{-13.27}$  per cent but the fit requires

a much higher dipole efficiency of  $\eta_{\text{dip}} = 83.60^{+15.65}_{-31.94}$  per cent and a narrow jet opening angle of  $1/f_B = 474^{+120}_{-180}$ . However, this fit has introduced a flare at roughly the 1000 s mark that could be indicative of overfitting.

**Table 9.** Parameters derived from the best-fitting models to the SGRBEE sample for  $n = 1$  and excluding data  $< 10$  s. Uncertainties represent a 95 per cent confidence interval. Values marked with an [L] are a parameter limit; those marked with an [F] were fixed during fitting.  $\chi^2_{\text{red}}$  values are shown to indicate goodness of fit. \*GRB 061210 has fewer data points than free parameters resulting in a negative  $\chi^2_{\text{red}}$  value.

GRB	$B$ ( $\times 10^{-15}$ G)	$P_i$ (ms)	$M_{D,i}$ ( $\times 10^{-2} M_{\odot}$ )	$R_D$ (km)	$\epsilon$	$\delta$	$\eta_{\text{dip}}$ (per cent)	$\eta_{\text{prop}}$ (per cent)	$1/f_B$	$\chi^2_{\text{red}}$
050724	$3.30^{+0.48}_{-0.36}$	$9.94^{+0.06}_{-0.26}$	$0.167^{+0.042}_{-0.028}$	$383^{+7}_{-7}$	$0.94^{+12.75}_{-0.83}$	$(0.85^{+3.15}_{-0.73}) \times 10^{-3}$	1[L]	$98^{+2}_{-8}$	$253^{+35}_{-22}$	5
051016B	$1.18^{+0.68}_{-0.48}$	$9.09^{+0.87}_{-2.84}$	$2.47^{+4.73}_{-1.63}$	$59^{+4}_{-3}$	$635.72^{+234.17}_{-216.98}$	$(1.00^{+0.91}_{-0.51}) \times 10^{-3}$	1[L]	$94^{+6}_{-20}$	$220^{+296}_{-144}$	2
051227	$8.86^{+1.10}_{-3.19}$	$4.00^{+1.66}_{-1.84}$	$0.67^{+1.84}_{-0.31}$	$134^{+35}_{-26}$	$4.98^{+456.99}_{-4.86}$	$(0.30^{+1.31}_{-0.30}) \times 10^{-1}$	5[F]	40[F]	$82^{+77}_{-57}$	2
060614	$6.21^{+0.41}_{-1.03}$	$8.30^{+1.14}_{-2.48}$	$0.755^{+0.453}_{-0.117}$	$1680^{+23}_{-23}$	$562.87^{+161.29}_{-103.91}$	$(1.00^{+0.14}_{-0.10}) \times 10^{-2}$	$84^{+15}_{-52}$	$8^{+2}_{-4}$	$506^{+91}_{-225}$	20
061006	$7.16^{+0.81}_{-1.07}$	$7.97^{+1.63}_{-3.97}$	$2.07^{+3.29}_{-0.56}$	$1908^{+89}_{-372}$	$136.05^{+94.65}_{-54.63}$	$20.98^{+7.99}_{-5.34}$	5[F]	40[F]	$380^{+209}_{-311}$	8
061210	$0.75^{+0.27}_{-0.24}$	$0.80^{+0.26}_{-0.11}$	$7.04^{+2.76}_{-2.20}$	$128^{+143}_{-42}$	$182.82^{+748.09}_{-165.31}$	$(1.47^{+6.69}_{-1.13}) \times 10^{-1}$	$7^{+3}_{-3}$	$91^{+9}_{-25}$	1[F]	-33*
070714B	$4.97^{+1.20}_{-1.45}$	$1.00^{+0.15}_{-0.27}$	$4.24^{+2.93}_{-0.90}$	$320^{+29}_{-25}$	$520.96^{+453.38}_{-494.48}$	$(1.55^{+0.92}_{-0.65}) \times 10^{-1}$	$48^{+42}_{-31}$	$80^{+19}_{-36}$	1[F]	2
071227	$8.40^{+1.52}_{-2.37}$	$1.79^{+1.99}_{-0.80}$	$4.98^{+4.42}_{-2.80}$	$250^{+25}_{-23}$	$1.78^{+28.53}_{-1.67}$	$(0.95^{+4.28}_{-0.61}) \times 10^{-3}$	5[F]	40[F]	$49^{+51}_{-33}$	2
080123	$7.08^{+0.18}_{-0.25}$	$0.91^{+0.07}_{-0.04}$	$9.84^{+0.16}_{-0.61}$	$254^{+5}_{-4}$	$62.03^{+117.14}_{-58.06}$	$(1.56^{+1.90}_{-1.19}) \times 10^{-4}$	$4^{+3}_{-3}$	$98^{+2}_{-9}$	1[F]	6
080503	$5.45^{+0.55}_{-1.29}$	$6.95^{+2.91}_{-4.62}$	$6.27^{+3.61}_{-5.58}$	$59^{+2}_{-5}$	$0.108^{+0.079}_{-0.008}$	$4.21^{+37.64}_{-2.15}$	$73^{+26}_{-54}$	$60^{+20}_{-36}$	1[F]	9
100212A	$9.98^{+0.02}_{-0.07}$	$7.50^{+2.39}_{-4.32}$	$9.96^{+0.04}_{-0.17}$	$163^{+1}_{-1}$	$980.05^{+19.22}_{-87.98}$	$(7.07^{+0.23}_{-0.62}) \times 10^{-1}$	$79^{+20}_{-20}$	$17^{+5}_{-4}$	$441^{+148}_{-94}$	19
100522A	$3.06^{+0.09}_{-0.07}$	$9.93^{+0.07}_{-0.33}$	$0.509^{+0.076}_{-0.105}$	$63^{+2}_{-1}$	$0.22^{+1.21}_{-0.11}$	$(3.11^{+2.10}_{-1.87}) \times 10^{-3}$	1[L]	$99^{+1}_{-3}$	$316^{+26}_{-19}$	37
111121A	$9.03^{+0.92}_{-2.25}$	$6.34^{+1.64}_{-2.71}$	$1.14^{+1.22}_{-0.31}$	$292^{+16}_{-14}$	$32.44^{+7.02}_{-5.21}$	$(1.77^{+0.36}_{-0.26}) \times 10^{-2}$	5[F]	40[F]	$247^{+119}_{-167}$	7
150424A	$9.19^{+0.68}_{-1.03}$	$8.99^{+0.97}_{-2.76}$	$0.544^{+0.421}_{-0.115}$	$434^{+61}_{-43}$	$20.40^{+9.75}_{-7.56}$	$(1.88^{+0.66}_{-0.59}) \times 10^{-2}$	$61^{+37}_{-45}$	$13^{+9}_{-9}$	$122^{+331}_{-69}$	2
160410A	$3.58^{+0.63}_{-0.95}$	$3.17^{+0.80}_{-1.43}$	$3.32^{+3.94}_{-0.89}$	$826^{+79}_{-87}$	$21.83^{+199.41}_{-19.02}$	$(3.65^{+5.63}_{-2.19}) \times 10^{-2}$	5[F]	40[F]	$410^{+181}_{-285}$	3

**Table 10.** AICc values for fits to the SGRBEE sample excluding data  $< 10$  s and using equation (14) for the dipole torque. \*GRB 061210 has fewer data points than free parameters and so these statistics should be treated with caution.

GRB	$p = 6$	$p = 7$	$p = 8$	$p = 9$
050724	5927	17 516	1636	<b>1287</b>
051016B	396	2327	444	<b>147</b>
051227	493	1000	192	<b>64</b>
060614	50 687	88 449	44 055	<b>43 667</b>
061006	294	854	424	<b>111</b>
061210*	372	1236	<b>96</b>	1532
070714B	880	3622	<b>212</b>	1402
071227	<b>115</b>	1293	161	202
080123	355	6162	752	<b>290</b>
080503	3186	13 299	<b>2336</b>	3670
100212A	9035	35 074	8757	<b>8037</b>
100522A	8709	22 489	8808	<b>6391</b>
111121A	2498	8441	898	<b>757</b>
150424A	398	5861	<b>252</b>	267
160410A	1198	1479	<b>717</b>	971

#### 5.4 Refitting excluding early-time data

The results presented in Table 7 are consistently pushing the upper bounds for the initial disc mass,  $M_{D,i}$ . This is most likely due to the model's need to have a high accretion rate at early times in order to reach the high luminosities at those times. Since the emission produced at these times is usually attributed to internal shocks and energy drawn from the merger rather than magnetic particle acceleration, fitting these high early-time luminosities may not strictly be within the remit of the model. We therefore chose to refit the sample excluding some of the early-time data.

We chose an arbitrary cut-off of 10 s to define the on-set of EE after the prompt emission. This meant we avoided making an arbitrary cut for each individual burst since EE is not currently well defined. The fits were performed for  $p = 6, 7, 8$  and  $9$  and  $n = 1$  for comparison with the work in Gompertz et al. (2014).

Table 8 presents the AICc values of the refits. The best fits (bold values) from Table 8 are plotted in Fig. 10 and the parameters derived from these fits are presented in Table 9 with the  $\chi^2_{\text{red}}$  goodness of fit statistic. GRB 061210 has very few data points and excluding data  $< 10$  s means that there are fewer data points than free parameters that resulted in negative AICc and  $\chi^2_{\text{red}}$  values. Therefore, it is shown here for consistency rather than as a statistically significant result.

As is shown in Fig. 10, the result of excluding the early-time data is to produce more light curves of the *humped* morphology than the *sloped* or *classic* variety in Fig. 6. But most surprisingly, this experiment did not succeed in reducing  $M_{D,i}$  as expected, suggesting the extra mass is a result of another change in the model, most likely the use of equation (13) instead of equation (14). Equation (14) enhances the dipole spin-down and mass-loss resulting in a lower initial disc mass.

#### 5.5 Refitting with enhanced dipole torque

For direct comparison with Gompertz et al. (2014), the sample was fitted once more using the enhanced dipole torque in equation (14) from Bucciantini et al. (2006) for  $n = 1$  and  $p = 6, 7, 8$  and  $9$ . The AICc values for the fits are presented in Table 10, the best fits from this table are shown in Fig. 11 and the parameters derived from those fits are presented in Table 11.

Including equation (14) in the model provides a marginal improvement in fitting, e.g. the tail of GRB 100212A is matched more

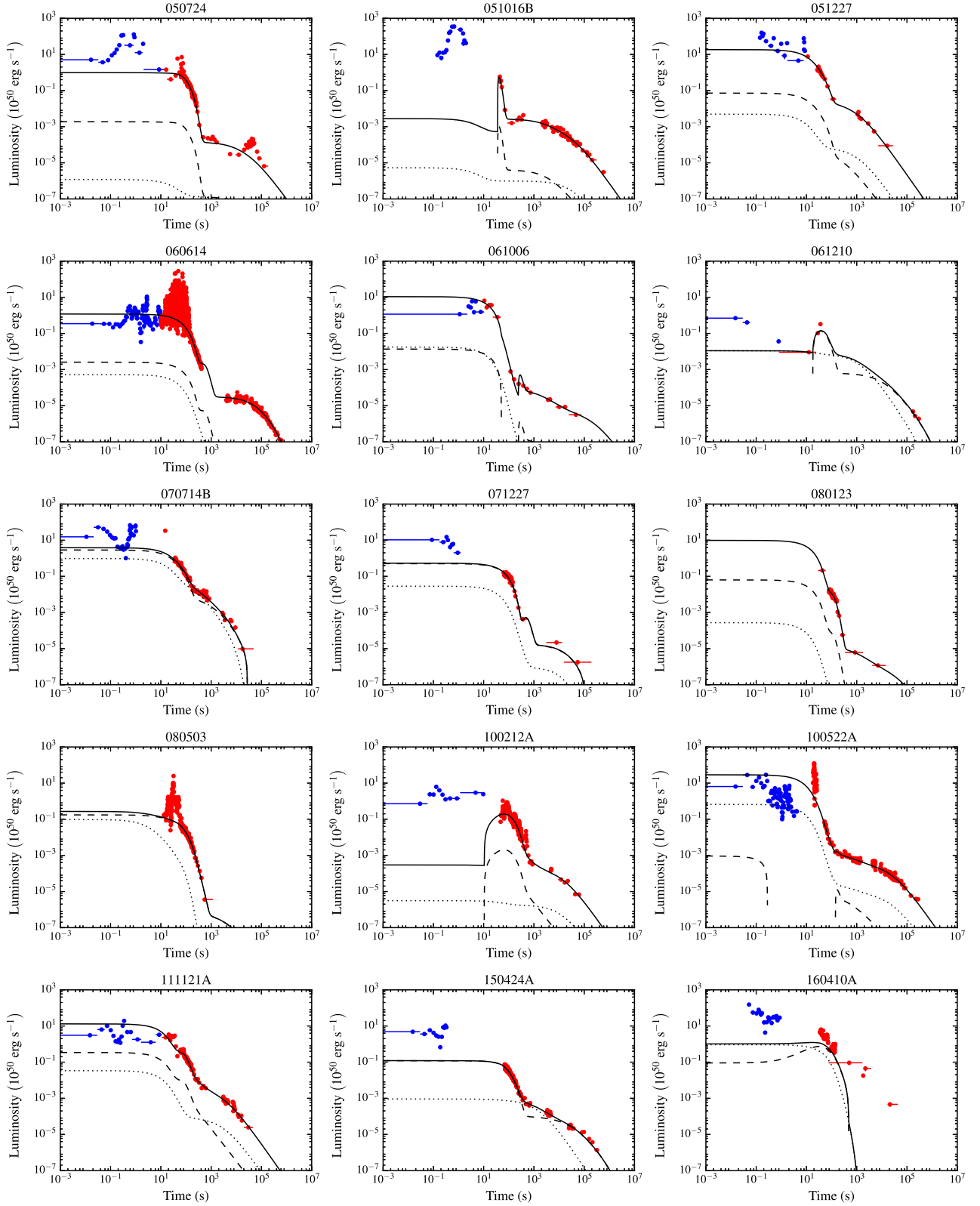


**Figure 11.** Results of fitting to the SGRBEE sample for the best global fits (bold values in Table 10) excluding data  $< 10$  s and using equation (14) for the dipole torque. Solid, black line – total luminosity; dashed, black line – propeller luminosity; dotted, black line – dipole luminosity. Data points are combined BAT and XRT data: blue points have been excluded from the fit, red points were included.



**Table 11.** Parameters derived from fits to SGRBEE sample for the global fits (bold values in Table 10) excluding data  $<10$  s and using equation (14) for the dipole torque. Uncertainties are a 95 per cent confidence interval and values marked with an [L] are a parameter limit. \*GRB 061210 has fewer data points than parameters resulting in a negative  $\chi^2_{\text{red}}$  value.

GRB	$B$ ( $\times 10^{15}$ G)	$P_i$ (ms)	$M_{D,i}$ ( $\times 10^{-2} M_{\odot}$ )	$R_D$ (km)	$\epsilon$	$\delta$	$\eta_{\text{dip}}$ (per cent)	$\eta_{\text{prop}}$ (per cent)	$1/f_B$	$\chi^2_{\text{red}}$
050724	$2.75^{+0.26}_{-0.31}$	$8.91^{+0.63}_{-1.12}$	$0.100^{+0.021}_{-0.005}$	$378^{+8}_{-8}$	$983.76^{+15.64}_{-67.62}$	$(5.70^{+1.15}_{-1.13}) \times 10^{-3}$	1[L]	$97^{+3}_{-10}$	$522^{+73}_{-128}$	5
051016B	$0.36^{+0.20}_{-0.09}$	$2.33^{+0.61}_{-0.57}$	$2.62^{+2.35}_{-1.56}$	$52^{+5}_{-2}$	$772.31^{+205.95}_{-259.35}$	$(4.15^{+5.45}_{-1.97}) \times 10^{-4}$	1[L]	$92^{+7}_{-23}$	$524^{+73}_{-213}$	2
051227	$8.12^{+1.80}_{-3.86}$	$4.91^{+3.23}_{-3.01}$	$0.26^{+0.87}_{-0.15}$	$159^{+60}_{-40}$	$13.32^{+732.02}_{-13.21}$	$(0.77^{+6.62}_{-0.77}) \times 10^{-2}$	$45^{+51}_{-36}$	$53^{+44}_{-44}$	$238^{+327}_{-187}$	2
060614	$3.03^{+0.36}_{-0.39}$	$6.05^{+1.60}_{-1.42}$	$0.31^{+0.13}_{-0.08}$	$1297^{+17}_{-17}$	$632.65^{+119.29}_{-105.42}$	$(1.53^{+0.14}_{-0.14}) \times 10^{-2}$	$80^{+19}_{-41}$	$19^{+10}_{-8}$	$383^{+208}_{-222}$	20
061006	$3.57^{+0.61}_{-0.75}$	$2.67^{+0.93}_{-1.02}$	$1.08^{+0.96}_{-0.36}$	$423^{+15}_{-14}$	$52.71^{+51.20}_{-29.47}$	$(2.38^{+0.65}_{-0.61}) \times 10^{-3}$	$73^{+26}_{-48}$	$6^{+6}_{-3}$	$347^{+240}_{-273}$	11
061210	$0.40^{+0.03}_{-0.03}$	0.69[L]	$1.19^{+0.25}_{-0.22}$	$211^{+89}_{-59}$	$815.21^{+177.54}_{-528.85}$	$(3.21^{+3.07}_{-0.88}) \times 10^{-1}$	$17^{+3}_{-3}$	$99^{+1}_{-3}$	1[F]	-43*
070714B	$1.77^{+0.17}_{-0.15}$	0.69[L]	$3.43^{+0.38}_{-0.82}$	$307^{+26}_{-22}$	$41.83^{+598.49}_{-21.04}$	$(1.21^{+0.92}_{-0.32}) \times 10^{-1}$	$75^{+24}_{-59}$	$99^{+1}_{-5}$	1[F]	2
071227	$1.19^{+0.27}_{-0.13}$	$0.70^{+0.04}_{-0.01}$	$5.46^{+0.20}_{-0.60}$	$1144^{+97}_{-116}$	$250.23^{+674.92}_{-225.49}$	$(0.20^{+1.25}_{-0.13}) \times 10^{-1}$	5[F]	40[F]	1[F]	3
080123	$8.31^{+1.61}_{-2.20}$	$5.67^{+2.71}_{-2.52}$	$0.32^{+0.38}_{-0.13}$	$244^{+7}_{-6}$	$54.14^{+91.66}_{-48.87}$	$(1.26^{+1.09}_{-0.60}) \times 10^{-4}$	$4^{+7}_{-3}$	$66^{+32}_{-40}$	$154^{+351}_{-112}$	6
080503	$9.10^{+0.87}_{-4.06}$	$1.06^{+0.74}_{-0.35}$	$0.75^{+0.92}_{-0.12}$	$767^{+23}_{-40}$	$36.89^{+828.92}_{-36.76}$	$(0.01^{+16.16}_{-0.01}) \times 10^{-1}$	$2^{+3}_{-1}$	$68^{+21}_{-43}$	1[F]	9
100212A	$0.73^{+0.08}_{-0.07}$	$3.91^{+0.37}_{-0.34}$	$0.11^{+0.02}_{-0.01}$	$550^{+15}_{-15}$	$0.37^{+0.95}_{-0.25}$	$(2.46^{+3.05}_{-1.34}) \times 10^{-2}$	1[L]	$77^{+21}_{-26}$	$94^{+50}_{-26}$	22
100522A	$1.53^{+0.29}_{-0.12}$	$0.74^{+0.15}_{-0.05}$	$8.45^{+1.22}_{-2.38}$	$243^{+6}_{-5}$	$18.73^{+10.36}_{-6.57}$	$(4.72^{+0.56}_{-0.50}) \times 10^{-3}$	$89^{+11}_{-24}$	1[L]	$43^{+22}_{-10}$	37
111121A	$2.21^{+0.26}_{-0.22}$	$1.45^{+0.34}_{-0.26}$	$1.97^{+0.64}_{-0.51}$	$247^{+15}_{-12}$	$0.20^{+0.73}_{-0.10}$	$(5.00^{+3.77}_{-3.18}) \times 10^{-2}$	$32^{+22}_{-24}$	$60^{+38}_{-44}$	$35^{+91}_{-18}$	6
150424A	$0.38^{+0.08}_{-0.07}$	$0.75^{+0.12}_{-0.05}$	$0.39^{+0.11}_{-0.04}$	$540^{+22}_{-21}$	$951.95^{+46.20}_{-168.74}$	$(5.13^{+0.88}_{-0.84}) \times 10^{-1}$	$2^{+1}_{-1}$	$91^{+9}_{-21}$	1[F]	2
160410A	$1.49^{+0.14}_{-0.13}$	0.69[L]	$0.17^{+0.53}_{-0.06}$	$544^{+563}_{-322}$	$0.57^{+6.17}_{-0.46}$	$20.42^{+22.88}_{-16.15}$	$99^{+1}_{-4}$	100[L]	1[F]	17

closely in Fig. 11 than Fig. 10, though in some cases it performs much worse, e.g. GRB 160410A. The initial disc mass  $M_{D,i}$  is reduced by approximately an order of magnitude across the sample. This is a reflection of the enhanced energy output facilitated by equation (14). Equation (14) does not produce a dramatic change in the morphology or energetics of the fits, nor does it significantly improve the fit statistics. However, the derived disc masses are more broadly in line with previous work (e.g. Rosswog 2007).

### 5.6 The $B$ - $P$ landscape

Fig. 12 shows where the results of this work fall in relation to other GRBs in both the long and short classifications. It needs to be noted that the results from Gompertz et al. (2014) used fixed efficiencies of  $\eta_{\text{dip}} = 5$  per cent and  $\eta_{\text{prop}} = 40$  per cent, whereas the work done in Rowlinson et al. (2013) uses 100 per cent efficiency instead, and our efficiencies have been free parameters in most fitting procedures. Also, Gompertz et al. (2014) used equation (14) that enhances the dipole spin-down and so these results appear to occupy their own region of low magnetic field and spin period. Hence, conclusions drawn from this plot require some caution.

However, Fig. 12 does show us that our results occupy a region of moderate to high magnetic field and spin period, indicating that the fallback accretion relaxes the constraints on the initial spin of the magnetar (i.e. it does not need to be born near the break-up period) since it will be spun up by the fallback regardless. Though this result could be due to either the addition of a  $t^{-5/3}$  fallback accretion profile or our inclusion of beaming as a fitting parameter. The results of this work still do not approach the same region as Gompertz et al. (2014) even when early-time, high-luminosity data is excluded and equation (14) is used which consolidates that the

shift in  $B$ - $P$  parameter space is due to the inclusion of fallback accretion.

## 6 CONCLUSIONS

We have modified the magnetar propeller model to include fallback accretion, examined the effect these changes have on model light curves and used an MCMC to fit the model to a sample of short GRBs exhibiting EE for a range of free parameters and ‘sharpness’ of propeller. We have found that the parameters derived from the fits produced by the propeller model with fallback accretion are consistent with theoretical predictions for magnetars.

Our model can cope with long, dipole plateaux and flare-like variability but struggles with the early-time, short-time-scale variability. However, since this variability is usually present in the prompt emission that is generally attributed to internal shocks rather than magnetic acceleration of particles, it is not strictly within the remit of the model to fit it.

The addition of fallback accretion provides a noticeable improvement in matching light curves compared to those presented in Gompertz et al. (2014) and fallback accretion may play a pivotal role in explaining the features of EE light curves. Our model uses a smoothed representation of fallback disc feeding as a simplest case scenario. A more ‘clumpy’ representation could potentially be more physical and useful to explain phenomena such as flares (Dall’Osso et al. 2017).

## ACKNOWLEDGEMENTS

The authors would like to thank the reviewers for their helpful and constructive comments. SLG would like to thank Dr Mark Wilkinson at the University of Leicester for many instructive

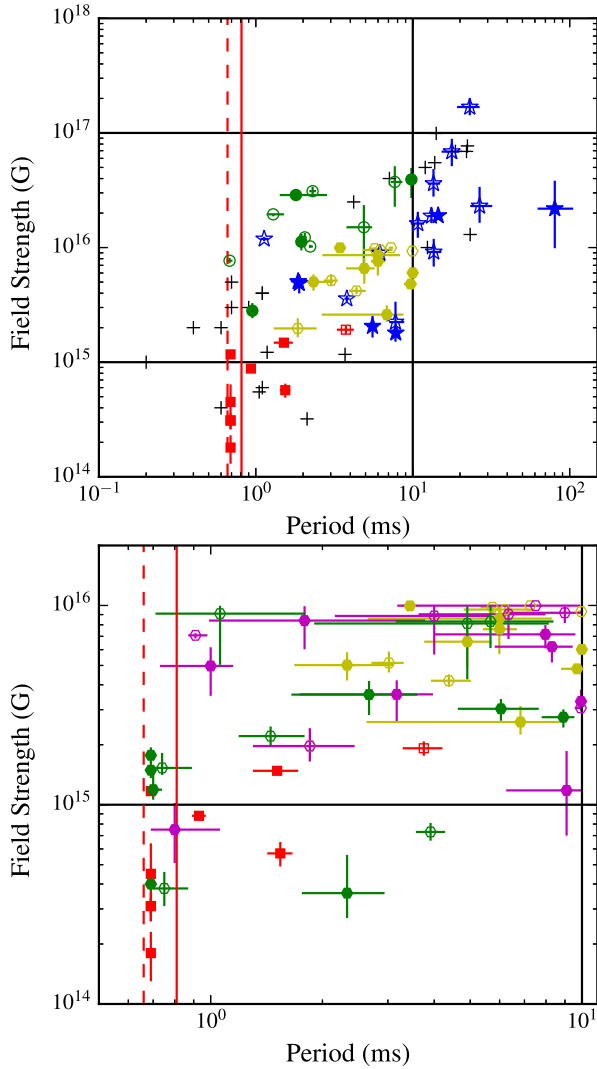


**Figure 12.** Plots of magnetic field strength versus initial spin period. The solid (dashed) red line represents the break-up period for a collapsar (binary merger) progenitor (Lattimer & Prakash 2004). Top panel – blue stars: stable magnetars and green circles: unstable magnetars that collapse to form a black hole (Rowlinson et al. 2013). Black ‘+’ symbols are the LGRB candidates identified by Lyons et al. (2010) and Dall’Osso et al. (2011). Red squares (both panels) show the values found in Gompertz et al. (2014). Yellow hexagons (both panels) represent the magnetic fields and initial spin periods of this work for the global best-fitting values in Table 7. Bottom panel – magenta hexagons are the  $B$  and  $P_1$  values for fits excluding data  $< 10$  s in Table 9; green hexagons are  $B$  and  $P_1$  values for fits excluding data  $< 10$  s and including equation (14) in Table 11. Filled symbols have observed redshifts, open symbols use the sample average redshift, which is  $z = 0.39$  for extended bursts and  $z = 0.72$  for the short bursts from Rowlinson et al. (2013).

conversations and acknowledge funding from the Weizmann Institute and the University of Leicester. PTO would like to acknowledge funding from STFC. This research used the Advanced Leicester Information Computational Environment (ALICE) High Performance Computing Facility at the University of Leicester. The work makes use of data supplied by the UKSSDC at the University of Leicester and the *Swift* satellite. *Swift*, launched in 2004 November, is a NASA mission in partnership with the Italian Space Agency and the UK Space Agency. *Swift* is managed by NASA Goddard. Penn State University controls science and flight operations from the Mission

Operations Centre in University Park, Pennsylvania. Los Alamos National Laboratory provides gamma-ray imaging analysis.

## REFERENCES

- Barkov M. V., Pozanenko A. S., 2011, MNRAS, 417, 2161  
 Barthelmy S. D. et al., 2005, Space Sci. Rev., 120, 143  
 Belczynski K., Perna R., Bulik T., Kalogera V., Ivanova N., Lamb D. Q., 2006, ApJ, 648, 1110  
 Berger E., 2007, ApJ, 670, 1254  
 Bloom J. S., Frail D. A., Sari R., 2001, ApJ, 121, 2879  
 Bromberg O., Nakar E., Piran T., Sari R., 2013, ApJ, 764, 179  
 Bucciantini N., Thompson T. A., Arons J., Quataert E., Del Zanna L., 2006, MNRAS, 368, 1717  
 Bucciantini N., Metzger B. D., Thompson T. A., Quataert E., 2012, MNRAS, 419, 1537  
 Burrows D. N. et al., 2005, Space Sci. Rev., 120, 165  
 Cannizzo J., Troja E., Gehrels N., 2011, ApJ, 734, 35  
 Cavanaugh J. E., Neath A. A., 2011, in Lovric M., ed., International Encyclopedia of Statistical Science. Springer, Berlin, p. 26  
 Cenko S., Kasliwal M., Cameron P., Kulkarni S., Fox D., 2006, GCN Circ., 5946, 1  
 Chapman R., Levan A. J., Priddey R. S., Tanvir N. R., Wynn G. A., King A. R., Davies M. B., 2007, in Napiwotzki R., Burleigh M. R., eds, ASP Conf. Ser. Vol. 372, 15th European Workshop on White Dwarfs. Astron. Soc. Pac., San Francisco, p. 415  
 Chincarini G. et al., 2010, MNRAS, 406, 2113  
 Curran P. A., Starling R. L. C., O’Brien P. T., Godet O., van der Horst A. J., Wijers R. A. M. J., 2008, A&A, 487, 533  
 D’Avanzo P., Fiore F., Piranomonte S., Covino S., Tagliaferri G., Chincarini G., Stella L., 2007, GCN Circ., 7152, 1  
 D’Avanzo P. et al., 2009, A&A, 498, 711  
 Dall’Osso S., Stratta G., Guetta D., Covino S., De Cesare G., Stella L., 2011, A&A, 526, A121  
 Dall’Osso S., Perna R., Tanaka T. L., Margutti R., 2017, MNRAS, 464, 4399  
 Evans P. A. et al., 2007, A&A, 469, 379  
 Evans P. A. et al., 2009, MNRAS, 397, 1177  
 Falcone A. D. et al., 2006, ApJ, 641, 1010  
 Foreman-Mackey D., Hogg D. W., Lang D., Goodman J., 2013, PASP, 125, 306  
 Frail D. A. et al., 2001, ApJ, 562, L55  
 Fruchter A. S. et al., 1999, ApJ, 519, L13  
 Gehrels N. et al., 2004, ApJ, 611, 1005  
 Giacomazzo B., Perna R., 2013, ApJ, 771, L26  
 Gompertz B. P., O’Brien P. T., Wynn G. A., Rowlinson A., 2013, MNRAS, 431, 293  
 Gompertz B. P., O’Brien P. T., Wynn G. A., 2014, MNRAS, 438, 240  
 Goodman J., Weare J., 2010, Commun. Appl. Math. Comput. Sci., 5, 65  
 Graham J. et al., 2009, ApJ, 698, 1620  
 Harrison F. A. et al., 1999, ApJ, 523, L121  
 Kaneko Y., Bostanci Z. F., Göğüş E., Lin L., 2015, MNRAS, 452, 824  
 Kouveliotou C., Meegan C. A., Fishman G. J., Bhat N. P., Briggs M. S., Koshut T. M., Paciesas W. S., Pendleton G. N., 1993, ApJ, 413, L101  
 Kumar P., Narayan R., Johnson J. L., 2008, MNRAS, 388, 1729  
 Lattimer J., Prakash M., 2004, Science, 304, 536  
 Lyons N., O’Brien P., Zhang B., Willingale R., Troja E., Starling R., 2010, MNRAS, 402, 705  
 MacKay D. J. C., 2003, Information Theory, Inference and Learning Algorithms. Cambridge Univ. Press, Cambridge  
 Mangano V. et al., 2007, A&A, 470, 105  
 Mereghetti S., Pons J. A., Melatos A., 2015, Space Sci. Rev., 191, 315  
 Mészáros P., 2006, Rep. Prog. Phys., 69, 2259  
 Metzger B. D., Quataert E., Thompson T. A., 2008, MNRAS, 385, 1455  
 Metzger B. D., Arcones A., Quataert E., Martínez-Pinedo G., 2010, MNRAS, 402, 2771  
 Norris J. P., Bonnell J. T., 2006, ApJ, 643, 266

- Norris J. P., Barthelmy S. D., Cummings J. R., Gehrels N., 2015, GCN Circ., 17759, 1
- Perley D. A. et al., 2009, ApJ, 696, 1871
- Piro A. L., Ott C. D., 2011, ApJ, 736, 108
- Price P. A., Berger E., Fox D. B., 2006, GCN Circ., 5275, 1
- Prochaska J., Bloom J., Chen H.-W., Hansen B., Kalirai J., Rich M., Richer H., 2005, GCN Circ., 3700, 1
- Rea N., Gullón M., Pons J. A., Perna R., Dainotti M. G., Miralles J. A., Torres D. F., 2015, ApJ, 813, 92
- Rhoads J. E., 1999, ApJ, 525, 737
- Roming P. W. A. et al., 2005, Space Sci. Rev., 120, 95
- Rosswog S., 2007, MNRAS, 376, L48
- Rosswog S., Ramirez-Ruiz E., Davies M. B., 2003, MNRAS, 345, 1077
- Rowlinson A., O’Brien P. T., Metzger B. D., Tanvir N. R., Levan A. J., 2013, MNRAS, 430, 1061
- Ryan G., Van Eerten H., MacFadyen A., Zhang B.-B., 2015, ApJ, 799, 3
- Sakamoto T. et al., 2016, GCN Circ., 19276, 1
- Sari R., Piran T., Halpern J. P., 1999, ApJ, 519, L17
- Selsing J. et al., 2016, GCN Circ., 19274, 1
- Shapiro S. L., Teukolsky S. A., 1983, Black Holes, White Dwarfs, and Neutron Stars: The Physics of Compact Objects. Wiley, New York
- Soderberg A. M., Berger E., Ofek E., 2005, GCN Circ., 4186, 1
- Xu D. et al., 2009, ApJ, 696, 971
- Zhang B., Yan H., 2011, ApJ, 726, 90
- Zhang B., Zhang B.-B., Liang E.-W., Gehrels N., Burrows D. N., Mészáros P., 2007, ApJ, 655, L25

This paper has been typeset from a  $\text{\TeX}/\text{\LaTeX}$  file prepared by the author.